



The Carnegie Supernova Project: Absolute Calibration and the Hubble Constant

Christopher R. Burns¹ , Emilie Parent² , M. M. Phillips³ , Maximilian Stritzinger⁴ , Kevin Krisciunas⁵ , Nicholas B. Suntzeff⁵, Eric Y. Hsiao⁶ , Carlos Contreras³ , Jorge Anais³, Luis Boldt³, Luis Busta³ , Abdo Campillay³, Sergio Castellón³, Gastón Folatelli^{3,7}, Wendy L. Freedman¹, Consuelo González³, Mario Hamuy⁸, Peter Heoflich⁶ , Wojtek Krzeminski¹¹, Barry F. Madore¹ , Nidia Morrell³ , S. E. Persson¹ , Miguel Roth³, Francisco Salgado³ , Jacqueline Serón⁹, and Simón Torres¹⁰

¹ Observatories of the Carnegie Institution for Science, 813 Santa Barbara St, Pasadena, CA 91101, USA

² Department of Physics and McGill Space Institute, McGill University, Montreal, QC H3A 2T8, Canada

³ Carnegie Institution of Washington, Las Campanas Observatory, Casilla 601, Chile

⁴ Department of Physics and Astronomy, Aarhus University, Ny Munkegade 120, DK-8000 Aarhus C, Denmark

⁵ George P. and Cynthia Woods Mitchell Institute for Fundamental Physics and Astronomy, Texas A&M University, Department of Physics and Astronomy, College Station, TX 77843, USA

⁶ Department of Physics, Florida State University, Tallahassee, FL 32306, USA

⁷ Facultad de Ciencias Astronómicas y Geofísicas, Universidad Nacional de La Plata, Instituto de Astrofísica de La Plata (IALP), CONICET, Paseo del Bosque S/N, B1900FWA La Plata, Argentina

⁸ Universidad de Chile, Departamento de Astronomía, Casilla 36-D, Santiago, Chile

⁹ Cerro Tololo Inter-American Observatory, Casilla 603, La Serena, Chile

¹⁰ SOAR Telescope, Casilla 603, La Serena, Chile

Received 2018 July 22; revised 2018 September 12; accepted 2018 September 22; published 2018 December 11

Abstract

We present an analysis of the final data release of the *Carnegie Supernova Project I*, focusing on the absolute calibration of the luminosity–decline rate relation for Type Ia supernovae (SNe Ia) using new intrinsic color relations with respect to the color-stretch parameter, s_{BV} , enabling improved dust extinction corrections. We investigate to what degree the so-called fast-declining SNe Ia can be used to determine accurate extragalactic distances. We estimate the intrinsic scatter in the luminosity–decline rate relation and find it ranges from ± 0.13 mag to ± 0.18 mag with no obvious dependence on wavelength. Using the Cepheid variable star data from the SH0ES project, the SN Ia distance scale is calibrated and the Hubble constant is estimated using our optical and near-infrared sample, and these results are compared to those determined exclusively from a near-infrared subsample. The systematic effect of the supernova’s host galaxy mass is investigated as a function of wavelength and is found to decrease toward redder wavelengths, suggesting this effect may be due to dust properties of the host. Using estimates of the dust extinction derived from optical and near-infrared wavelengths and applying these to the H band, we derive a Hubble constant $H_0 = 73.2 \pm 2.3$ km s^{−1} Mpc^{−1}, whereas using a simple $B - V$ color correction applied to the B band yields $H_0 = 72.7 \pm 2.1$ km s^{−1} Mpc^{−1}. Photometry of two calibrating SNe Ia from the CSP-II sample, SN 2012ht and SN 2015F, is presented and used to improve the calibration of the SN Ia distance ladder.

Key words: cosmological parameters – distance scale – dust, extinction – supernovae: general

Supporting material: machine-readable tables

1. Introduction

The successful use of Type Ia supernovae (SNe Ia) as extragalactic distance indicators hinges on the discovery that the rate of evolution of their light curves (i.e., decline rate) is correlated with their intrinsic luminosity (Pskovskii 1977; Phillips 1993). Since this initial discovery, a handful of different parameters have been used to characterize the decline rate, including $\Delta m_{15}(B)$ (Phillips 1993), the light-curve stretch (Perlmutter et al. 1999), the Multi-Color Light Curve Shapes (MLCS) parameter Δ (Riess et al. 1996; Jha et al. 2007), and the Spectral Adaptive Light curve Template (SALT) stretch-like parameter x_1 (Guy et al. 2005). One problem common to all these parameters, however, is their difficulty in working with what seems to be a separate class of SNe Ia, the so-called fast decliners, which are often conflated with the spectrally classified 1991bg-like objects (Filippenko et al. 1992; Leibundgut et al. 1993). In this paper, we use the recently

proposed color-stretch parameter, s_{BV} , (Burns et al. 2014) as a way forward to deal with fast-declining SNe Ia.

Another key ingredient to using SNe Ia to infer distances is the ability to correct for dust extinction. The simplest approach is to perform a one-parameter color correction, as reddening is directly proportional to extinction (Cardelli et al. 1989; Fitzpatrick 1999). This was first done by Tripp (1998), and we refer to it hereafter as the Tripp method. The disadvantage of this approach is that it allows one to determine only a combination of luminosity and a color (a reddening-free luminosity). While this is treated as a nuisance parameter in cosmology, the luminosities of SNe Ia are important to determine in order to study the physics of their explosion mechanisms (Ashall et al. 2014; Hoefflich et al. 2017). In a previous paper (Burns et al. 2014), we developed a method to determine more accurate extinction corrections. In this paper, we apply this method to calibrate the luminosity–decline rate relation (Phillips et al. 1999) and compare the results with the calibration based on the Tripp method.

One of the major goals of the *Carnegie Supernova Project I* (hereafter CSP-I; Hamuy et al. 2006) was to produce a

¹¹ Deceased.

photometrically homogeneous set of SNe Ia of exceptional quality. While an obvious application of such a sample is for cosmology and measuring the Hubble constant H_0 , the high cadence and small photometric errors of CSP-I were not necessary for a statistical sample to anchor the Hubble diagram. Indeed, the publication history of the CSP is skewed much more toward the physics of the SNe and their environments, rather than constraining cosmological parameters. Now that the final data release (DR3) of the CSP-I is published (see Krisciunas et al. 2017), we present an analysis of the intrinsic luminosities of the entire sample and a derivation of H_0 tied to a Cepheid distance scale. This paper is a continuation of previous work on the intrinsic colors of SNe Ia that allowed us to properly deal with dust extinction and produce an improved luminosity–decline rate relation. As part of that analysis, we use the color-stretch parameter s_{BV} (Burns et al. 2014). As we demonstrate below, s_{BV} is a more reliable light-curve parameter when fitting the fast-declining SNe Ia (i.e., those for which $\Delta m_{15}(B) > 1.7$ mag), both in predicting the shapes of the optical and near-infrared (NIR) light curves and in producing better behaved intrinsic colors as a function of decline rate. We shall now forge ahead in using s_{BV} as an intrinsic SN Ia luminosity indicator.

In the preliminary analysis paper (Folatelli et al. 2010), we used an assumed value of the Hubble constant in order to calibrate the luminosities of the CSP-I sample. In this paper, we use Cepheid variables from the SH0ES project (Riess et al. 2016) to solve for the absolute calibration of the SN Ia luminosities as a function of decline rate and measure the Hubble constant. In particular, we investigate the systematics involved in using different reddening corrections, different subsamples of SNe Ia, and different wavelength ranges (e.g., optical versus NIR).

The paper is organized follows. Section 2 briefly describes the CSP-I sample and the photometric system used. Section 3 reviews s_{BV} and compares it with other existing parameters. Section 4 presents the absolute calibration of the CSP-I DR3 for fixed values of the Hubble constant, H_0 , using both a simple color correction and a method that estimates a proper dust extinction. In Section 5, Cepheid data from the SH0ES project (Riess et al. 2016) are used to calibrate the distances to 19 SN Ia host galaxies and to determine H_0 . Section 6 concludes with a summary of our results.

2. The CSP-I DR3 Sample

The final CSP-I data release is presented by Krisciunas et al. (2017). For the purposes of this paper, we briefly describe the sample, underlining aspects important for this work.

DR3 consists of 134 SNe Ia observed between 2004 and 2009. The majority of the objects were observed in optical ($ugriBV$) and NIR (YJH) passbands, and at least some visual-wavelength spectra were obtained for most of the objects (e.g., Folatelli et al. 2010). The sample contains objects with redshifts spanning the range of $0.004 < z < 0.083$. The CSP-I was purely a follow-up program of SNe discovered by other surveys using the facilities of Las Campanas Observatory with the goal of minimizing systematics due to calibration and extinction. Our primary source of objects was the Lick Observatory Supernova Survey (Filippenko et al. 2001), which, being a targeted survey, is biased toward luminous hosts.

The philosophy for the CSP-I observations was “quality over quantity.” We chose to follow up fewer objects, but with higher

cadence and signal-to-noise ratio than most other follow-up projects. This allowed us to construct accurate light-curve template models as a function of decline rate (Burns et al. 2011), while the wide wavelength coverage allowed us to model the intrinsic colors and extinctions (Burns et al. 2014). The CSP-I also produced high-fidelity filter functions using a monochromator (Rheault et al. 2010; Stritzinger et al. 2011), which improves S- and K-corrections (Stritzinger et al. 2005) and allows accurate determination of absolute zero-points for the photometric natural system (Krisciunas et al. 2017). The net result was a high-quality set of SNe Ia classified by decline rate and having redshift- and extinction-corrected light curves. These are crucial for determining distances and producing accurate Hubble diagrams.

2.1. Sample Used for Cosmology

Of the 134 objects in the CSP-I DR3 sample, 123 are *bona fide* SNe Ia. The remaining 11 objects are members of peculiar subtypes and have been omitted from our analysis:

1. SN 2005hk, SN 2008ae, SN 2008 ha, SN2009J and SN 2010ae are all 2002cx-like SNe (Li et al. 2001);
2. SN 2007if and SN 2009dc are Super Chandrasekhar (SC) candidates (Howell et al. 2006);
3. SN 2006bt and SN 2006ot are peculiar objects and form their own subgroup (Foley et al. 2010; Stritzinger et al. 2011) and are relatively easy to identify with NIR photometry (Phillips 2012);
4. SN 2005gj and SN 2008J are 2002ic-like SNe Ia (Hamuy et al. 2003) that exhibit signatures of interaction (i.e., prevalent Balmer emission lines) produced from the SN ejecta shocking circumstellar material.

We also eliminate three normal SNe Ia: SN 2006dd, SN 2007so, and SN 2008bd, whose CSP-I observations begin well after maximum, when their light curves are in their linear decline phase and for which template light-curve fits are unreliable. In summary, this leaves us with 120 CSP-I SNe Ia to use in our analysis. In order to anchor the SN Ia distance ladder, we also use 14 SNe Ia from the literature. Finally, three SNe Ia from the CSP-II project (Phillips et al. 2018) have Cepheid distances and are included in this analysis. The photometry for SN 2012fr is published in Contreras et al. (2018), while the photometry for SN 2012ht and SN 2015F is presented in Appendix A. This brings the total number of SN Ia anchors to 19, which is the same set used by Riess et al. (2016).

Each supernova is fit with light-curve templates using the SNooPy (Burns et al. 2011) package, yielding estimates of s_{BV} and the maximum brightness m_X in each filter X . SNooPy also applies K-corrections to remove the effects of redshift. The pseudocolors derived from the maximum brightnesses are used to estimate extinctions using the methods of Burns et al. (2014; see Section 4.2). Visual representations of the fits of all of the CSP-I SNe are presented in Krisciunas et al. (2017).

3. The Color-stretch Parameter s_{BV}

The use of s_{BV} was motivated by the problem $\Delta m_{15}(B)$ has in measuring the decline rate of the fastest-declining objects. Once beyond $\Delta m_{15}(B) \sim 1.7$ mag, the transition from the initial decline to the linear decline occurs before day 15, which causes $\Delta m_{15}(B)$ to be less sensitive to the rate of evolution of

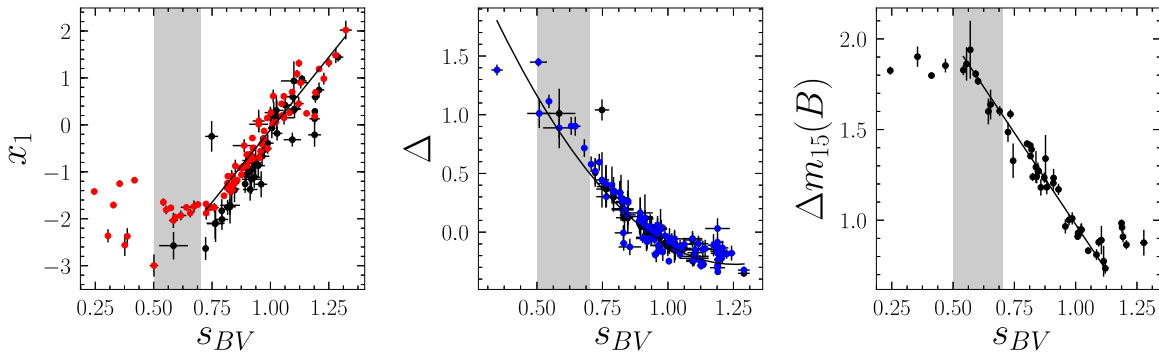


Figure 1. Comparison of different light-curve parameters as a function of the color stretch s_{BV} . A low value of s_{BV} indicates a faster declining and hence less luminous SN. Left panel: the SALT2 x_1 parameter. Black points are from Hicken et al. (2009), and red points are from Burns et al. (2014). Middle: the MLCS2k2 Δ parameter. Black points are from Hicken et al. (2009), and blue points are from Jha et al. (2007). Right: the decline rate $\Delta m_{15}(B)$ from the CSP-I DR3 sample. In all three panels, the relations from Equations (1)–(3) are shown as solid black lines. Gray rectangles show the range of s_{BV} where the simple relations with respect to x_1 and $\Delta m_{15}(B)$ break down, and one might consider them as the transition region between normal and fast-declining SNe Ia.

the B -band light curve (Phillips 2012; Burns et al. 2014). This transition was initially used by Pskovskii (1977) as a way to define a decline rate for SNe Ia, but it proved too impractical and was never adopted by others. Höflich et al. (2010) also attempted to fix the problem by applying a stretch to the light curves and then measuring a “stretched” $\Delta m_{15,s}$.

Another very pronounced feature is the time at which the SN Ia reaches its reddest color. For the well-behaved $B - V$ colors, this usually takes place ~ 30 days after B maximum, but occurs earlier for fast decliners and later for slow decliners. Together with the time of maximum light for the SN Ia, this provides a kind of clock for measuring how fast the object is evolving. For convenience, we use the time between B maximum and $(B - V)$ maximum, but other filters could also be used. Dividing by 30 days yields a stretch-like parameter for which $s_{BV} \sim 1$ for “normal” SNe Ia, while fast decliners typically have $s_{BV} < 0.5$. Unlike $\Delta m_{15}(B)$, s_{BV} is insensitive to extinction (Phillips et al. 1999). And unlike $\Delta m_{15}(B)$, the correlation between time of $(B - V)$ maximum and the shape of the optical and NIR light curves does not break down for the fast decliners (Burns et al. 2014). This is a significant improvement over the templates introduced in the first version of SNooPy (Burns et al. 2011), which used $\Delta m_{15}(B)$ as a light-curve shape parameter.

There are theoretical reasons to believe that s_{BV} might prove to be a better diagnostic of the intrinsic brightness of SNe Ia. The location of the peak $(B - V)$ color is generally thought to be due to the recombination of Fe III to Fe II, which deposits energy into the ejecta, making it bluer (Kasen 2006; Höflich et al. 2017) and producing the secondary maxima in the NIR bands. Recombination occurs when the ejecta have cooled to a particular temperature, and the temporal phase when this occurs depends on the total energy deposited into the ejecta and the time-dependent opacity, both of which depend on the amount of ^{56}Ni generated during the thermonuclear disruption (see, e.g., Höflich et al. 2017). The amount of ^{56}Ni itself is also thought to be the primary determinant of the luminosity of the SN Ia (Arnett 1982).

3.1. Comparison with Other Light Curve Parameters

We briefly consider how s_{BV} compares with the other most commonly used light-curve parameters: $\Delta m_{15}(B)$, Δ , and x_1 . In particular we are interested in analytic formulas that enable the conversion between one light-curve parameter to another, but

also a measure of the rms scatter in these relations. While template light-curve fitters can measure statistical errors using standard methods when fitting for the decline rate, they tend to be very small due to the precision of the photometry and the large number of points being fit by a single-parameter function. Determining the systematic error is not so obvious. However, if we compare several different estimators of the decline rate, the scatter will give us an indication of the systematic error introduced by the fitting process.

Comparing s_{BV} with $\Delta m_{15}(B)$ is straightforward, as these are direct measurements from the B and V light curves themselves. We use the light-curve analysis package SNooPy (Burns et al. 2011) to interpolate each light curve with a Gaussian process interpolator (Rasmussen & Williams 2006). These are used to measure the time of B maximum, $\Delta m_{15}(B)$, and the epoch of $(B - V)$ maximum. We also use SNooPy to compute and apply K-corrections (Oke & Sandage 1968) for each light curve using the Hsiao et al. (2007) spectral template. In the right panel of Figure 1, we plot the results and a linear fit over the range $0.6 < s_{BV} < 1.2$. Interestingly, it appears that $\Delta m_{15}(B)$ flattens out at the slow-declining end as well as at the fast end. Wherever these relations flatten out (or go vertical) is a regime where one parameter is potentially telling us more than the other and could therefore prove to be a better discriminator of the decline rate.

For the other two commonly used shape parameters, we use the values of Δ and x_1 published by their authors. For x_1 we also used SALT2 to fit some CSP-I objects to show how x_1 fails in the same way as $\Delta m_{15}(B)$: at high decline rates, the relation flattens out.¹¹ In contrast, the MLCS2k2 parameter Δ shows a very clear correlation for the fast decliners, but begins to flatten out at the slow end. This is to be expected, since Δ is defined as a brightness correction relative to a “standard” SN Ia, so the middle panel of Figure 1 is simply a scaled version of the luminosity–decline rate relation in the V band. In no case do any of these relations become vertical: s_{BV} seems to be more informative than the other three parameters. Nevertheless, it is useful to be able to compare these parameters, so we derive analytic relations between s_{BV} and each of the other three parameters. This is done using simple χ^2 minimization. Fitting a linear relation for x_1 , we obtain

$$x_1 = -0.10(0.03) + 6.2(0.2)(s_{BV} - 1). \quad (1)$$

¹¹ To be fair, SALT2 was never meant to be used to fit fast decliners.

This relation is valid for $s_{BV} > 0.7$. The rms dispersion is 0.27 in x_1 or 0.04 in s_{BV} .

Unlike x_1 , the relation between Δ and s_{BV} is quite continuous over the entire range and shows no obvious break point. Nevertheless, the relation flattens at larger s_{BV} , so we fit a quadratic:

$$\Delta = -0.11(0.02) - 1.28(0.08)(s_{BV} - 1) + 2.5(0.2)(s_{BV} - 1)^2, \quad (2)$$

which is valid for the entire range of s_{BV} . The rms dispersion is 0.11 mag in Δ or 0.08 in s_{BV} .

Finally, the relation between s_{BV} and $\Delta m_{15}(B)$ is found to be

$$\Delta m_{15}(B) = 0.98(0.01) - 2.02(0.05)(s_{BV} - 1), \quad (3)$$

and this is valid over the range $0.5 < s_{BV} < 1.15$. The rms dispersion is 0.06 mag in $\Delta m_{15}(B)$ or 0.03 in s_{BV} .

Given these three independent measures of the decline rate for SNe Ia, we can take the average rms of the fits to Equations (1)–(3) as indicative of the systematic error in s_{BV} for any *one* object, which is $\sigma(s_{BV}) = 0.05$. When fitting the decline rate relation for cosmological purposes, this will become a random error added in quadrature to the statistical errors reported by SNooPy.

4. Intrinsic Luminosities

Having presented s_{BV} , which quantifies the relative luminosity of SNe Ia, we now turn to the other parameter needed to determine distances: the extinction. A commonly used technique to handle the extinction is the Wesenheit function (Madore 1982). In Folatelli et al. (2010), we presented this calibration as the Tripp method and will continue to use this name. The advantage of this method is that for a fixed value of R_V , the correction removes the effects of extinction without needing to know the intrinsic colors. However, the assumption of constant R_V (also labeled β in other analyses, e.g., Guy et al. 2007) is demonstrably not correct in our own Milky Way galaxy (Cardelli et al. 1989; Fitzpatrick 1999; Nataf 2015), or in the host galaxies of SNe Ia (Riess et al. 1996; Mandel et al. 2011; Burns et al. 2014). Furthermore, if one is interested in the intrinsic luminosity of SNe Ia, then a proper treatment of the extinction is necessary, including variations in the reddening curve from host to host. In this section, we discuss the inference of the reddening correction, the luminosity–decline rate relation, and the possibility of using the fast-declining SNe Ia as standardizable candles.

4.1. Tripp Calibration

For a single set of three filters labeled X , Y , and Z , which define a magnitude in band X and $Y - Z$ color, the Tripp method models the observed peak magnitude m_X as

$$m_X = P_{XYZ}^N(s_{BV} - 1) + \mu(z_{\text{cmb}}, H_0, C) + R_{XYZ}(m_Y - m_Z) + \alpha_M(\log_{10} M_*/M_\odot - M_0), \quad (4)$$

where $P_{XYZ}^N(s_{BV} - 1)$ is a polynomial of order N as a function of $s_{BV} - 1$, and $\mu = \mu(z_{\text{cmb}}, H_0, C)$ is the distance modulus given a set of cosmological parameters C including H_0 . Here, R_{XYZ} can be interpreted either as a simple parameter to be

determined in the fitting or, if one assumes a reddening law, as

$$R_{XYZ} = \frac{R_X}{R_Y - R_Z}, \quad (5)$$

where each term is a function only of R_V through the reddening law (e.g., Cardelli et al. 1989; Fitzpatrick 1999). A special case, the combination $XYZ = BBV$, yields $R_{BBV} = R_V$ because $R_B = R_V + 1$. Using Equation (5), one can fit multiple filter triplet combinations simultaneously and solve for a single R_V . The final term of Equation (4) takes into account the correlation between the host galaxy stellar mass and intrinsic luminosity of its SN Ia (Neill et al. 2009; Kelly et al. 2010; Sullivan et al. 2010; Uddin et al. 2017) with α_M being the slope of the correlation and M_0 an arbitrary mass zero point, which we take to be $M_0 = 10^{11} M_\odot$. We derive host stellar masses for the CSP-I sample in Appendix B. It is important to point out, though, that any estimate of host mass will involve the distance to the host. This introduces a serious covariance in host mass with Hubble residual and must be handled carefully when doing inference using Equation (4). Specifically, since $\log_{10}(M_*/M_\odot) \propto 0.4\mu$ (see Appendix B), the covariance will be $\text{cov}(\mu, \log_{10}(M_*/M_\odot)) = 0.4\delta\mu^2$, where $\delta\mu$ is the error in distance. We take this into account explicitly by including the distance dependence in $\log_{10} M_*/M_\odot$ (see Equation (12)).

A serious drawback of this approach is that both intrinsic (i.e., physics of the SN explosion) and extrinsic (dust extinction) sources of color variation are conflated into a single correction, so the inferred value of R_V cannot reflect the true average dust properties. Recent work by Mandel et al. (2017) shows that these effects can be separated in a statistical sense, alleviating the bias introduced in determining R_V . For the purposes of this paper, we will not attempt to separate these effects in the Tripp method. Instead we tackle the problem by using more sophisticated color models to properly separate reddening and intrinsic color variations (see Section 4.2).

4.1.1. Calibration

We fit Equation (4) (and all other models later in this paper) using a Markov chain Monte Carlo (MCMC) method. The sampling of the MCMC chains is done using the “No U-Turn Sampler” provided by the data modeling language STAN (Carpenter et al. 2017). Four parallel chains with different initial positions in parameter space were produced to check for convergence using the Gelman–Rubin statistic \hat{R} (Gelman & Rubin 1992). This statistic, which estimates the ratio of the variance of a parameter across the four chains to the average variance within the chains, converges to $\hat{R} = 1$ typically within 500 iterations, which are discarded. More chains could be employed to better estimate \hat{R} , but since we are only using it as a convergence test, four are sufficient.

The distance modulus is computed from the redshift of the host galaxy using standard Λ CDM cosmology and a fixed $H_0 = 72 \text{ km s}^{-1} \text{ Mpc}^{-1}$, density parameter $\Omega_m = 0.27$, and cosmological constant parameter $\Omega_\Lambda = 0.73$ to be consistent with Folatelli et al. (2010). We will introduce H_0 as a free parameter later in Section 5. We leave the reddening parameter R_V as a free parameter. The error in each data point is modeled as a combination of photometric error $\sigma_{X,i}$, intrinsic dispersion

σ_X for each filter X , and a distance error, σ_μ :

$$\sigma = \sqrt{\sigma_{X,i}^2 + \sigma_X^2 + \sigma_\mu^2}. \quad (6)$$

The error σ_μ is due to peculiar velocities and is incurred when the distance modulus is derived from the Hubble law. Unlike σ_X , this extra dispersion term is achromatic and scales with redshift, $\sigma_\mu \propto \frac{v_{\text{pec}}}{z}$, where we allow the peculiar velocity v_{pec} to vary as a free parameter. Because the contribution of σ_μ decreases rapidly with redshift, its value will be constrained by the scatter at low redshift, and the intrinsic dispersions σ_X will be constrained by the scatter at higher redshift. The existence of coherent flows (Neill et al. 2007) could potentially increase σ_X . This will be investigated in an upcoming CSP paper, where we will leverage the increased redshift range of the CSP-II sample.

In summary, we use MCMC to fit the observed magnitudes at the maximum of our SNe Ia by solving for the following parameters: the coefficients of the polynomial P_{XYZ}^N describing the shape of the Tripp-corrected magnitudes as a function of s_{BV} , the slope of the $X - Y$ color correction R_{XYZ} , the intrinsic scatter in each band σ_X , the peculiar velocity v_{pec} , and the slope of the luminosity–host mass correlation α_M . We assume uniform priors on all parameters, except for σ_X , where we impose a strictly positive uniform prior.

We investigate the effects of restricting our sample to only objects with blue colors ($B - V < 0.5$) and also whether we can fit the fast-declining objects ($s_{BV} < 0.5$) with a single linear or higher-order polynomial relation.

It should be noted that in cases where a magnitude in filter X is corrected by a color constructed with the same filter (e.g., B corrected with $B - V$), the appropriate error must be added to the off-diagonal elements of the covariance matrix. This will ensure that errors are propagated properly. For example, degenerate cases, like including both combinations B, B, V and V, B, V , will not improve the constraints on the model parameters any more than B, B, V alone. We can also fit single X, Y, Z combinations alone and obtain color coefficients that are independent of the form of the reddening law $R_X(R_V)$. We choose to fit a second-order polynomial ($N=2$) for all color combinations. For some (e.g., BBV), the quadratic term is negligible, whereas in the case of the others (e.g., YBV), a quadratic term is significant. We find that, in particular, a quadratic term is needed for the NIR bands in order to fit the fast-declining objects.

The Tripp relations for the fits using the combinations $(X, Y, Z) = (B, B, V)$ and $(X, Y, Z) = (H, B, V)$ are shown in Figure 2. In general, we recover many of the qualitative aspects that have been seen before (Krisciunas et al. 2004; Folatelli et al. 2010; Kattner et al. 2012), namely that both the stretch and color corrections decrease steadily with longer wavelength. However, we find that all of the NIR stretch corrections are inconsistent with zero slope and curvature. In other words, even at NIR wavelengths, SNe Ia are not perfect standard candles. Table 1 shows the best-fit values for the polynomial P_{XYZ}^2 under the same circumstances we used when fitting the intrinsic colors, namely, omitting the fast-declining or reddest SNe Ia.

4.2. Intrinsic Colors and Reddening Corrections

Since extinction can only make objects redder, there will be a “blue edge” to the distribution of observed colors. However,

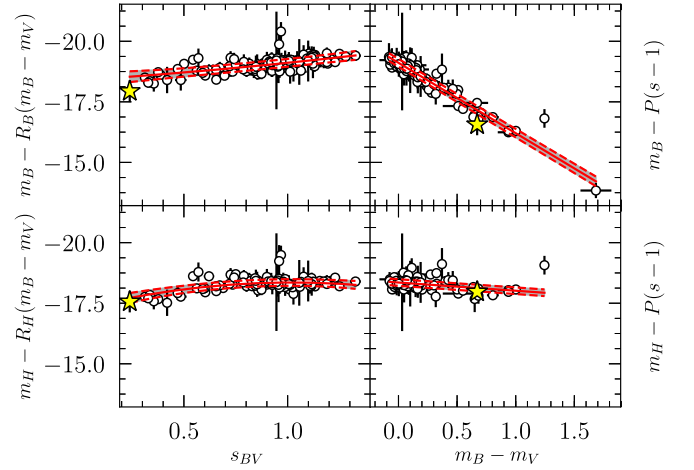


Figure 2. Comparison of the Tripp calibration in B and H correcting by $(B - V)$ color. The top row shows the B band, and the bottom row shows the H band. The left column shows absolute magnitudes corrected for color as a function of s_{BV} , while the right column shows absolute magnitudes corrected for s_{BV} as a function of $(B - V)$ color. The red solid lines show the best-fit polynomial, and the dashed red lines show the $\pm\sigma_X$ intrinsic dispersion. The yellow star corresponds to SN 2006mr, which is the fastest declining object in our sample and whose distance is inferred from three normal SNe Ia that were hosted by the same galaxy, NGC 1316.

there is a strong dependence of the intrinsic color with decline rate of SNe Ia (Phillips 1993), so we must find blue edges in the color– s_{BV} planes (see Figure 3).

This was done in Burns et al. (2014) by simultaneously solving for the color excess $E(B - V)$ and reddening slope R_V of each SN Ia as well as the intrinsic colors (i.e., blue edges), which were modeled as a quadratic function of s_{BV} . With the increased number of objects in DR3, particularly at low s_{BV} (i.e., fast decliners), we discovered that using a more complex fitting function was necessary in order to adequately fit the intrinsic colors.

For this paper, we replace the quadratic function with basis splines. This allows for a more complex behavior of the intrinsic colors as a function of decline rate and is simple to implement in the STAN modeling language used to do the fits. Figure 3 shows a comparison between these two models for the intrinsic colors. We use the same methodology as Burns et al. (2014), the only difference being the functional form of the intrinsic colors. The largest discrepancies between the quadratic and spline models are for the slowly declining ($s_{BV} > 1.2$) events. Due to the small number of objects at the slow end, one object (SN 2005hj) tends to pull the solution (we have plotted this object with red points in Figure 3). SN 2005hj has been shown to have a peculiar Si II $\lambda 6355$ velocity evolution, similar to SN 2000cx (Quimby et al. 2007), which may explain its peculiar colors. However, the CSP-II SN 2012fr also shows a similarly flat Si II $\lambda 6355$ evolution (Contreras et al. 2018) and yet has a normal decline rate ($s_{BV} = 1.12$) and colors (plotted as blue points in Figure 3), so we do not feel justified in excluding it. In Table 2, we list updated extinction values for the entire CSP-I sample that will be used in this paper. The details of how the basis splines are constructed and the values of the best-fit coefficients can be found in Appendix C.

Table 1
Tripp Fit Parameters

X	P^0 (mag)	P^1 (mag)	P^2 (mag)	R_{XBV}	R_V	α (mag/dex)	σ_X (mag)	v_{pec} (km s $^{-1}$)
Full sample								
B	−19.182(062)	−0.89(11)	−0.02(30)	2.81(09)	1.65(08)	−0.063(031)	0.13	310
V	−19.181(061)	−0.89(11)	−0.02(30)	1.82(09)	1.65(08)	−0.063(030)	0.13	310
u	−18.818(097)	−1.28(17)	0.32(44)	3.64(13)	1.13(52)	−0.135(051)	0.22	233
g	−19.229(084)	−0.90(11)	−0.13(31)	2.38(09)	1.57(09)	−0.073(032)	0.13	317
r	−19.099(059)	−0.74(10)	0.38(27)	1.38(08)	1.78(08)	−0.077(028)	0.12	302
i	−18.523(059)	−0.48(10)	0.41(27)	0.98(08)	1.85(09)	−0.081(028)	0.12	295
Y	−18.517(077)	−0.07(11)	1.19(30)	0.42(09)	1.34(21)	−0.083(032)	0.12	284
J	−18.633(062)	−0.37(12)	0.61(32)	0.36(10)	1.27(36)	−0.056(029)	0.11	336
H	−18.431(062)	−0.05(12)	1.18(31)	0.27(09)	1.28(57)	−0.050(030)	0.11	299
$B - V < 0.5$								
B	−19.161(062)	−0.94(11)	−0.36(43)	2.70(15)	1.54(14)	−0.053(030)	0.13	238
V	−19.161(061)	−0.94(11)	−0.37(44)	1.70(15)	1.54(14)	−0.052(030)	0.13	238
u	−18.793(095)	−1.35(18)	−0.47(64)	3.63(14)	1.12(51)	−0.117(050)	0.21	197
g	−19.206(082)	−0.97(11)	−0.57(43)	2.28(15)	1.48(14)	−0.064(032)	0.13	245
r	−19.081(060)	−0.77(10)	0.12(41)	1.27(14)	1.67(13)	−0.069(028)	0.13	233
i	−18.501(060)	−0.52(10)	−0.10(41)	0.93(14)	1.79(17)	−0.072(029)	0.13	245
Y	−18.497(076)	−0.10(11)	0.34(41)	0.57(15)	1.69(35)	−0.070(031)	0.12	222
J	−18.601(062)	−0.43(11)	−0.42(45)	0.43(16)	1.51(58)	−0.047(029)	0.11	284
H	−18.400(062)	−0.10(12)	0.17(47)	0.27(14)	1.33(85)	−0.046(030)	0.11	248
$s_{BV} > 0.5$								
B	−19.159(062)	−0.93(12)	−0.61(43)	2.80(09)	1.64(09)	−0.053(030)	0.13	329
V	−19.159(061)	−0.94(11)	−0.62(43)	1.80(09)	1.64(09)	−0.052(031)	0.13	328
u	−18.790(097)	−1.32(18)	−0.35(70)	3.60(11)	1.10(45)	−0.122(052)	0.22	232
g	−19.204(084)	−0.96(12)	−0.80(43)	2.37(10)	1.56(09)	−0.064(033)	0.13	334
r	−19.081(060)	−0.77(11)	−0.05(39)	1.36(08)	1.76(08)	−0.069(029)	0.12	317
i	−18.499(059)	−0.52(10)	−0.21(38)	0.96(08)	1.82(10)	−0.071(028)	0.12	309
Y	−18.480(076)	−0.11(11)	0.32(42)	0.35(09)	1.18(22)	−0.076(031)	0.11	280
J	−18.593(060)	−0.44(12)	−0.35(45)	0.29(10)	1.02(36)	−0.048(029)	0.11	330
H	−18.394(061)	−0.10(12)	0.13(47)	0.19(08)	0.82(52)	−0.046(030)	0.11	295
$s_{BV} > 0.5$ and $B - V < 0.5$								
B	−19.162(061)	−0.94(11)	−0.30(46)	2.71(15)	1.55(14)	−0.053(030)	0.13	241
V	−19.163(061)	−0.94(11)	−0.31(46)	1.71(15)	1.55(14)	−0.053(031)	0.13	240
u	−18.796(095)	−1.35(17)	−0.42(69)	3.63(14)	1.12(51)	−0.118(050)	0.21	198
g	−19.207(083)	−0.96(11)	−0.53(46)	2.28(16)	1.48(15)	−0.064(032)	0.13	247
r	−19.083(060)	−0.77(10)	0.17(42)	1.28(14)	1.68(13)	−0.069(029)	0.13	236
i	−18.501(061)	−0.52(10)	−0.10(43)	0.92(15)	1.78(17)	−0.072(029)	0.13	248
Y	−18.489(075)	−0.10(10)	0.15(42)	0.53(15)	1.59(35)	−0.073(031)	0.12	217
J	−18.598(063)	−0.43(12)	−0.48(47)	0.41(16)	1.48(57)	−0.047(029)	0.11	284
H	−18.395(061)	−0.11(12)	0.03(48)	0.26(14)	1.24(84)	−0.046(030)	0.11	246

Note. P^0 , P^1 , and P^2 are the coefficients of the zeroth-, first-, and second-order terms of the polynomial $P_{XYZ}^N(s_{BV} - 1)$ from Equation (4).

4.3. The Reddening Model

With estimates of extinction, we can now replace the simple color term in Equation (4) with a proper reddening correction. It has been known for some time (Phillips 1993; Hamuy et al. 1995; Phillips et al. 1999) that the intrinsic colors of SNe Ia are a function of decline rate, with the fast decliners being redder than slow decliners. In contrast to previous analysis (Folatelli et al. 2010), Burns et al. (2014) found that the relation between intrinsic colors and s_{BV} required a quadratic function rather than a linear one. It is therefore likely that the absolute magnitudes of SNe Ia would also be quadratic in s_{BV} . We therefore propose the following model for the observed magnitudes of our sample of SNe Ia:

$$m_X = P_X^N(s_{BV} - 1) + \mu(z_{\text{cmb}}, H_0, C) + R_X(R_V)E(B - V) + \alpha_M(\log_{10} M_*/M_\odot - M_0). \quad (7)$$

Here, m_X is the observed magnitude in filter X ; P_X^N is an order- N polynomial in $s_{BV} - 1$, representing the luminosity–decline rate relation; $\mu(z_{\text{cmb}}, H_0, C)$ is the distance modulus for a given redshift z_{cmb} ; $R_X(R_V)$ is the total-to-selective absorption coefficient for filter X as a function of the reddening parameter R_V ; and $E(B - V)$ is the color excess. The values of R_V and $E(B - V)$, as well as their errors and covariances, were computed using the methods of Burns et al. (2014). We fit all objects in all filters simultaneously using MCMC and obtain estimates of the following parameters: the coefficients of the polynomial describing the luminosity–decline rate relation P_X^N , intrinsic scatter in each filter σ_X , the slope of the host-galaxy mass relation α_M , and the average peculiar motion v_{pec} . As in Section 4.1.1, we hold the Hubble constant H_0 and cosmological parameters C fixed and also solve for a correlation with host galaxy mass. In Section 5, we will incorporate SNe Ia with

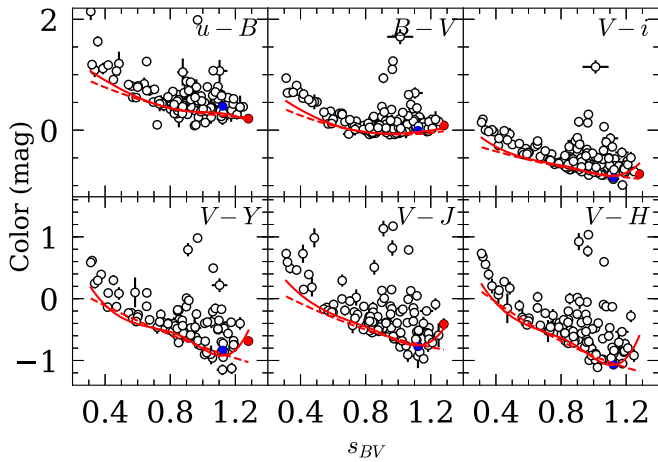


Figure 3. Plot of observed colors of the CSP-I SNe Ia DR3 sample. Extinction can only cause points to increase in color, so the intrinsic colors are defined by the blue edges of these distributions. The models for these intrinsic colors are plotted as red lines. The solid red line represents the best-fit spline function of s_{BV} , whereas the dashed red line is the polynomial fit from Burns et al. (2014). The red point corresponds to SN 2005hj, while the blue point is SN 2012fr.

independent distance estimates in order to constrain H_0 . When dealing with the extinction, we could correct the observed magnitudes m_X in Equation (7) and construct a covariance matrix to handle the resulting correlated errors. However, since v_{pec} and σ_X must also be included in the diagonal terms of the covariance matrix, it would have to be recomputed and inverted at each MCMC step. Instead, a more computationally efficient approach is to treat $E(B - V)$ and R_V as nuisance parameters with Gaussian priors determined from Section 4.2. In this way, we account for the uncertainty and covariance due to the extinction without having to invert large matrices. Table 3 summarizes the best-fit parameters using several different subsets of the data.

Figure 4 shows the results of fitting the absolute magnitudes as a function of both s_{BV} and $\Delta m_{15}(B)$. While there is a slight decrease in the rms scatter of the fits using s_{BV} as shape parameter rather than Δm_{15} for the normal objects ($s_{BV} > 0.5$, $\Delta m_{15}(B) < 1.7$ mag), there is a marked improvement in fitting the faster decliners, which appear to be a more continuous extension of the normal (albeit quadratic) luminosity–decline rate relation, perhaps suggesting a single explosion mechanism (e.g., Hoefflich et al. 2017). The question then arises: can the use of s_{BV} as a shape parameter allow the use of these objects as better standardizable candles than with $\Delta m_{15}(B)$?

4.4. Results

Using the information from our intrinsic color analysis, namely the best-fit values of $E(B - V)$ and R_V , we can correct for the extinction and solve for absolute luminosities rather than color-corrected luminosities as we did in Section 4.1.1. We fit Equation (7) for each SN Ia and each filter X simultaneously. We use the same priors for the luminosity–decline rate relation coefficients, intrinsic dispersions, distance moduli, and peculiar velocities as we did with the Tripp analysis. An important difference, however, is that each SN must be corrected for extinction using the values of $E(B - V)$ and R_V determined from the colors. Even though this introduces two additional degrees of freedom for each and every SN Ia, there are typically nine data points (filters) to be fit, and the

extinction parameters were constructed without knowledge of the distances. So while it is likely the scatter will be reduced (see Figure 5), the overall trend with s_{BV} is not a function of how we fit the intrinsic colors.

Figure 5 shows a comparison of the residuals of both the Tripp and reddening-corrected fits (left and middle panels, respectively) for a sample of three filters (u , B , and H). As expected, the magnitude of these residuals increases at low redshift because peculiar velocities are the dominant source of variance. The red lines show the combination of error due to a peculiar velocities and an intrinsic dispersion in each filter, whose values are tabulated in Table 3.

It is quite striking how much the dispersion is reduced in B when using reddening-corrected magnitudes rather than a simple color correction, while the dispersions in u and H seem to be unchanged. This is because, while exploring parameter space, the MCMC chains will tend to favor values of $E(B - V)$ and R_V that minimize the residuals in the luminosity–decline rate relation, resulting in a posterior whose mean is shifted with respect to that of the input prior. These shifts have to be small compared to the widths of their uncertainties and must simultaneously improve the fit for all filters observed for each object. These small shifts have virtually no effect on the redder wavelengths, so H appears unchanged in Figure 5. For u , the shifts required to improve the fit end up increasing the scatter in the other optical filters, so the overall likelihood is lower, suggesting that the scatter is real and not just errors in the reddening correction. This is expected for u , where intrinsic differences from SN to SN have long been known to be larger in the near-UV and UV (Foley & Kasen 2011; Burns et al. 2014) and our photometry tends to be of poorer quality.

4.5. Cross-validation

To more accurately measure the dispersion in the luminosity–decline rate relation and how minimizing the distance residuals can affect the extinction estimates, we use the technique of cross-validation, where the calibration of the luminosity–decline rate relation is done while omitting a fraction of the training sample. The resulting calibration can then be used to predict the distance of the omitted SNe Ia. Comparing these cross-validated distances with the Hubble distance then gives us a more realistic measure of the scatter one can expect when using a single SN Ia to measure a host distance. The cross-validated distances can also be used for the nearest objects whose Hubble distances are uncertain due to peculiar velocities. For simplicity, we use “leave one out” cross-validation (LOOCV), where the calibration is recomputed after omitting each SN in turn.

The resulting histogram of distance residuals is then fit with a Gaussian mixture model in order to robustly measure the dispersion and also identify outliers (Hogg et al. 2010; Krisciunas et al. 2017). Briefly, the residual of object i is assumed to originate from two Gaussian distributions: one with probability q_i , centered at zero and with standard deviation equal to the model errors (see Equation (6)), and a second with probability $1 - q_i$ and having an unknown center and standard deviation. The result is a more realistic estimate of σ_X (which we will call σ_{CV}) and a “quality” parameter q_i for each SN that ranges from zero to one. Low values of q_i indicate high probability of the SN being an outlier. The values of σ_{CV} are given in Table 3, and the values of q_i for each SN are given in Table 2.

Table 2
Properties of CSP-I and Calibration SNe Ia

SN Name	z_{hel}	z_{cmb}	s_{BV}	$\Delta m_{15}(B)$ (mag)	$m_{V,\text{max}}$ (mag)	$E(B - V)$ (mag)	R_V	$\text{cov}(E, R)^a$	μ_{CV} (mag)	$\langle q_i \rangle$
1981B	0.00603	0.00717	0.921(031)	1.140(062)	11.886(007)	0.147(023)	1.7(5)	−0.0065	30.89(15)	0.98
1990N	0.00300	0.00407	1.122(031)	0.961(061)	12.677(007)	0.128(016)	2.3(7)	−0.0021	31.78(29)	0.92
1994ae	0.00400	0.00512	1.046(031)	0.918(061)	13.073(008)	0.187(018)	1.7(7)	−0.0042	32.09(26)	0.98
1995al	0.00500	0.00588	1.126(034)	0.891(061)	13.213(008)	0.182(017)	2.0(7)	−0.0031	32.29(23)	0.94
1998aq	0.00370	0.00426	0.949(030)	1.046(060)	12.433(006)	0.025(012)	2.0(3)	−0.0008	31.55(27)	0.95
2001el	0.00390	0.00368	0.952(031)	1.052(061)	12.653(006)	0.291(016)	2.2(3)	−0.0029	31.26(27)	0.98
2002fk	0.00712	0.00661	0.979(030)	1.044(079)	13.269(006)	0.030(011)	2.6(2)	−0.0024	32.45(16)	0.98
2003du	0.00638	0.00665	1.006(030)	0.979(060)	13.534(004)	0.025(013)	1.0(3)	−0.0063	32.84(16)	0.98
2004dt	0.01972	0.01881	1.189(032)	1.104(061)	15.068(022)	0.149(025)	2.7(7)	−0.0003	33.94(08)	0.15
2004ef	0.03097	0.02977	0.816(030)	1.331(060)	16.733(003)	0.162(016)	1.8(5)	−0.0038	35.53(05)	0.98
2004eo	0.01569	0.01473	0.818(030)	1.314(060)	15.063(008)	0.130(025)	1.1(7)	−0.0098	33.96(07)	0.97
2004ey	0.01578	0.01463	1.010(030)	0.967(060)	14.820(002)	0.026(018)	1.3(3)	−0.0074	34.12(07)	0.97
2004gc	0.03208	0.03211	0.923(038)	1.079(076)	16.576(046)	0.226(051)	1.9(8)	−0.0095	35.38(09)	0.93
2004gs	0.02663	0.02750	0.689(030)	1.557(060)	16.969(005)	0.190(014)	1.9(4)	−0.0027	35.49(05)	0.98
2004gu	0.04583	0.04690	1.250(032)	0.823(061)	17.280(009)	0.097(031)	1.0(7)	−0.0048	36.64(04)	0.98
2005A	0.01913	0.01834	0.963(032)	1.057(064)	17.117(015)	1.165(021)	1.7(1)	−0.0013	34.37(07)	0.97
2005M	0.02200	0.02297	1.208(030)	0.796(060)	15.907(002)	0.055(020)	2.0(0)	−0.0028	35.19(05)	0.98
2005W	0.00888	0.00795	0.923(031)	1.111(062)	14.034(006)	0.232(019)	1.9(6)	−0.0041	32.82(15)	0.97
2005ag	0.07937	0.08002	1.190(031)	0.916(060)	18.443(005)	0.031(018)	1.6(3)	−0.0024	37.82(04)	0.98
2005al	0.01239	0.01329	0.858(030)	1.340(060)	14.936(005)	0.009(009)	1.6(3)	−0.0019	34.07(07)	0.96
2005am	0.00789	0.00897	0.725(030)	1.490(060)	13.619(004)	0.078(016)	1.1(8)	−0.0060	32.45(10)	0.84
2005be	0.03500	0.03560	0.760(035)	1.455(073)	16.914(039)	0.032(022)	1.7(3)	−0.0019	35.88(05)	0.98
2005bg	0.02307	0.02416	1.002(040)	1.023(079)	15.828(037)	0.075(029)	1.9(8)	−0.0021	35.04(07)	0.98
2005bl	0.02404	0.02511	0.387(032)	1.906(061)	17.806(022)	0.330(033)	1.9(6)	−0.0052	35.06(09)	0.97
2005bo	0.01389	0.01501	0.850(031)	1.293(063)	15.423(005)	0.333(016)	2.2(5)	−0.0032	33.79(10)	0.94
2005cf	0.00646	0.00704	0.970(031)	1.039(102)	13.210(007)	0.093(019)	2.3(6)	−0.0062	32.33(15)	0.98
2005el	0.01490	0.01489	0.838(030)	1.352(060)	14.943(007)	0.007(008)	1.5(4)	−0.0031	34.04(07)	0.97
2005eq	0.02896	0.02835	1.122(032)	0.813(060)	16.241(006)	0.109(017)	2.4(6)	−0.0054	35.40(04)	0.98
2005hc	0.04591	0.04498	1.193(031)	0.875(061)	17.305(004)	0.037(017)	2.4(2)	−0.0004	36.64(04)	0.96
2005hj	0.05797	0.05695	1.280(034)	0.796(062)	17.695(009)	0.027(034)	1.3(3)	−0.0088	37.05(04)	0.98

Note.

^a The covariance between $E(B - V)$ and R_V .

(This table is available in its entirety in machine-readable form.)

For each SN Ia, we have two estimates of $E(B - V)$ and R_V : those determined from the color analysis of Section 4.2 (when distance is not considered) and those we get as posteriors from the MCMC while calibrating the luminosity–decline rate relation (where distance is included). Figure 6 shows how the differences in these estimates are correlated with the residuals in the distance. In all cases, the shift is small compared to the width of the prior on the variable (indicated by horizontal error bars). Nonetheless, the resulting change in B -band extinction (right panel of Figure 6) is comparable to the scatter in the luminosity–decline rate relation and therefore will artificially reduce the measured intrinsic scatter. Note, however, that there is no systematic bias: just as many points are shifted to low values of $E(B - V)$ and R_V as are shifted to high values.

Another important result of this cross-validation analysis is that the dispersion in the residuals σ_{CV} is quite uniform for all of the filters, save for u , which is consistently ~ 0.1 mag larger. Also, combining multiple filters does not reduce the scatter relative to using individual filters, indicating that the residuals are highly correlated, which is not surprising as the dominant source should be peculiar velocities (which is an achromatic error) and uncertainties in the reddening parameters.

We include the cross-validated measures of σ_X in Table 3. These should be used when considering the error in distance one can expect when using the reddening method as a distance

measure. We also include the average quality parameter $\langle q_i \rangle$ and cross-validated distance modulus μ_{CV} for each SN in Table 2.

4.6. Fast Decliners

We turn once again to the question of whether the fast-declining objects for which $s < 0.5$ can be incorporated into the modeling of the luminosity of SNe Ia. Looking at Figure 2, it seems that a quadratic fit to the luminosity as a function of decline rate is adequate to capture the behavior for $s_{BV} < 0.5$. A linear relation can account for the luminosity of the fast decliners in the B band. In the case of the H band, however, the points with $s_{BV} < 0.5$ lie systematically below the linear fit, and a quadratic term is required. While the fast-declining objects are intrinsically dimmer than the normal SNe Ia, they are also significantly redder, and the Tripp color correction compensates in the optical. However, in the NIR, the correction is smaller and the fast decliners remain below the linear relation in Figure 2. This indicates that the reason fast-declining SNe Ia are red is likely not due to dust but rather that they are intrinsically red.

In contrast, Figure 4 shows a very smooth and continuous decline rate relation for all objects, albeit requiring a significantly nonlinear functional fit. Nevertheless, it is striking that such a relation seems to apply to the full range of s_{BV} . Unfortunately, being intrinsically faint, we have few fast-declining events that

Table 3
Absolute Magnitude Fit Parameters

Filter	P^0 (mag)	P^1 (mag)	P^2 (mag)	α (mag dex $^{-1}$)	σ_X (mag)	σ_{CV} (mag)	v_{pec} (km s $^{-1}$)
Full sample							
<i>B</i>	−19.422(063)	−0.83(11)	3.76(28)	−0.084(030)	0.11	0.15	262
<i>V</i>	−19.352(059)	−0.89(10)	2.47(26)	−0.072(028)	0.10	0.15	259
<i>u</i>	−19.106(086)	−1.14(16)	5.08(39)	−0.175(046)	0.17	0.24	309
<i>g</i>	−19.448(090)	−0.87(11)	3.06(28)	−0.092(033)	0.11	0.13	268
<i>r</i>	−19.216(059)	−0.75(10)	2.32(24)	−0.081(027)	0.10	0.14	260
<i>i</i>	−18.589(063)	−0.49(11)	1.83(26)	−0.083(031)	0.12	0.15	282
<i>Y</i>	−18.568(098)	−0.06(14)	1.89(30)	−0.087(040)	0.15	0.15	254
<i>J</i>	−18.670(071)	−0.32(15)	1.25(35)	−0.057(035)	0.13	0.16	343
<i>H</i>	−18.450(070)	−0.06(14)	1.61(30)	−0.046(036)	0.13	0.14	292
$s_{BV} > 0.5$							
<i>B</i>	−19.392(061)	−0.89(11)	2.76(41)	−0.076(029)	0.10	0.16	283
<i>V</i>	−19.329(059)	−0.93(10)	1.73(40)	−0.066(028)	0.10	0.14	275
<i>u</i>	−19.062(086)	−1.25(16)	3.62(62)	−0.157(045)	0.16	0.23	283
<i>g</i>	−19.416(084)	−0.93(11)	2.07(41)	−0.081(031)	0.10	0.13	302
<i>r</i>	−19.196(060)	−0.78(10)	1.72(39)	−0.076(027)	0.10	0.14	267
<i>i</i>	−18.565(064)	−0.53(11)	1.08(42)	−0.073(031)	0.12	0.15	273
<i>Y</i>	−18.541(099)	−0.09(14)	1.04(52)	−0.073(041)	0.15	0.16	218
<i>J</i>	−18.640(068)	−0.42(14)	0.20(54)	−0.049(035)	0.12	0.17	322
<i>H</i>	−18.425(069)	−0.09(14)	0.64(54)	−0.045(036)	0.12	0.15	285
$E(B - V) < 0.5$							
<i>B</i>	−19.404(058)	−0.82(10)	3.69(26)	−0.079(027)	0.10	0.15	249
<i>V</i>	−19.335(056)	−0.88(09)	2.39(23)	−0.067(025)	0.09	0.14	245
<i>u</i>	−19.096(087)	−1.14(16)	5.07(40)	−0.175(046)	0.17	0.24	329
<i>g</i>	−19.429(081)	−0.86(10)	2.96(26)	−0.083(029)	0.09	0.13	211
<i>r</i>	−19.202(058)	−0.75(09)	2.26(22)	−0.076(025)	0.09	0.14	247
<i>i</i>	−18.577(062)	−0.48(10)	1.78(24)	−0.083(030)	0.12	0.14	260
<i>Y</i>	−18.548(086)	−0.05(12)	1.80(27)	−0.078(035)	0.13	0.15	250
<i>J</i>	−18.653(067)	−0.32(14)	1.17(32)	−0.052(032)	0.12	0.16	283
<i>H</i>	−18.435(066)	−0.07(13)	1.53(28)	−0.041(034)	0.12	0.15	271
$s_{BV} > 0.5$ and $E(B - V) < 0.5$							
<i>B</i>	−19.369(057)	−0.90(10)	2.53(37)	−0.068(026)	0.09	0.15	254
<i>V</i>	−19.307(056)	−0.94(09)	1.51(35)	−0.059(024)	0.08	0.14	257
<i>u</i>	−19.046(086)	−1.25(16)	3.50(63)	−0.156(044)	0.16	0.24	253
<i>g</i>	−19.394(075)	−0.94(09)	1.82(35)	−0.072(026)	0.07	0.13	253
<i>r</i>	−19.177(057)	−0.78(09)	1.53(35)	−0.070(025)	0.09	0.14	245
<i>i</i>	−18.547(063)	−0.52(10)	0.92(40)	−0.072(030)	0.11	0.15	244
<i>Y</i>	−18.515(087)	−0.10(12)	0.77(45)	−0.065(035)	0.12	0.16	232
<i>J</i>	−18.616(065)	−0.43(13)	−0.04(48)	−0.042(031)	0.11	0.16	285
<i>H</i>	−18.403(065)	−0.12(13)	0.41(50)	−0.039(033)	0.11	0.15	259

Note. P^0 , P^1 , and P^2 are the coefficients of the zeroth, first-, and second-order terms of the polynomial $P_X^N(s_{BV} - 1)$ from Equation (7).

are sufficiently distant to ascertain how well the relation does at the very extreme end of the decline rate relation. But for one object, SN 2006mr, which is the fastest declining object in our sample, we are fortunate that the host galaxy (NGC 1316) hosted three other SNe Ia that are not part of the CSP-I training sample (Stritzinger et al. 2010). We therefore have an independent distance estimate of $\mu = 31.25 \pm 0.04$ mag. This allows us to place SN 2006mr in Figures 2 and 4, which we distinguish using a yellow star symbol. The trend with s_{BV} continues smoothly for the fastest object, and SN 2006mr lies very close to the extrapolated luminosity–decline rate relation. More quantitatively, we can compare the distance to NGC 1316 with the cross-validated distance for SN 2006mr with fixed $H_0 = 72$ km s $^{-1}$ Mpc $^{-1}$ (to be consistent with Stritzinger et al. 2010): $\mu_{06mr} = 31.26 \pm 0.16$ mag. In contrast, using $\Delta m_{15}(B)$ as a predictor would lead to distance estimates up to a magnitude more distant.

Lastly, it is worth noting that the right-hand panel of Figure 4 shows a dispersion very similar to the left-hand side, showing again that the true value of s_{BV} primarily lies in how it sorts the fast-declining objects. What looks like a very fast drop-off of the decline rate relation for $\Delta m_{15}(B) > 1.7$ mag is in reality just a failure of the parameter to accurately classify how fast an SN Ia evolves.

5. The Hubble Constant

In Sections 4.1.1 and 4.3, we left H_0 as a fixed parameter, thereby setting the distance scale of the universe. In order to allow H_0 to vary in our simulations and infer its most likely value, we must use independent distance estimates to the closest SNe Ia. In principle, any method can be used, but Cepheid variables have been the primary calibrator (Freedman et al. 2001; Sandage et al. 2006; Riess et al. 2016). Cepheids have the advantage of a long history in the literature and have

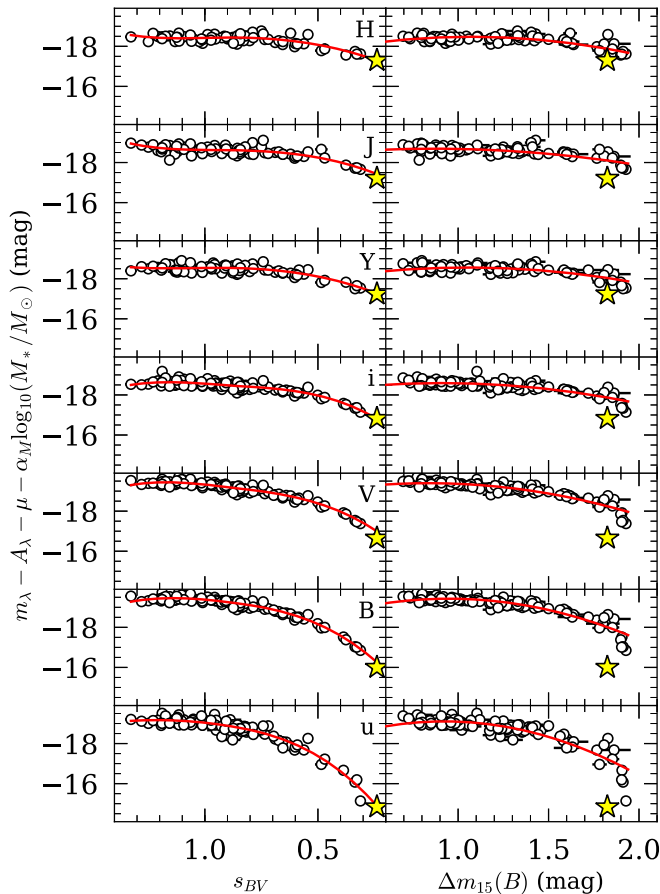


Figure 4. Luminosity–decline rate relation for the CSP-I DR3 SN Ia sample. The left-hand panels show the absolute magnitude of the SNe Ia as a function of s_{BV} , whereas the right-hand panels show the absolute magnitudes as a function of $\Delta m_{15}(B)$. The yellow star corresponds to the fastest declining object in the DR3 sample, SN 2006mr, adopting the distance of NGC 1316 derived from three other normal SNe Ia (Stritzinger et al. 2010).

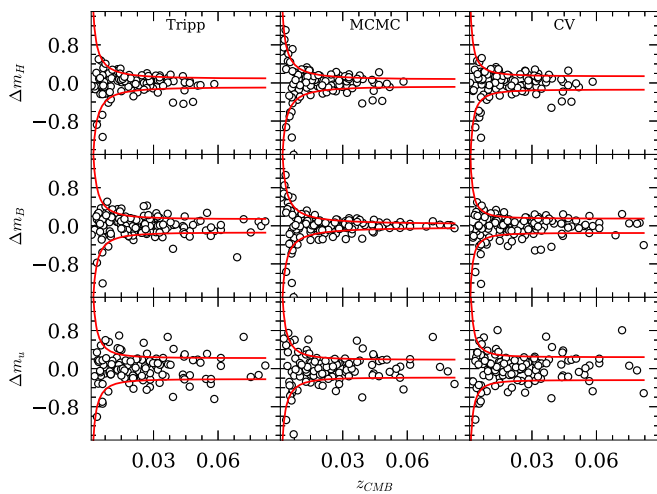


Figure 5. Model residuals as a function of redshift. The left panels show the residuals for a Tripp color correction, the middle panels for a reddening correction incorporating knowledge of the distance, and the right panels for a reddening correction using cross-validation where the distance is unknown. The three rows show residuals in three different filters: u , B , and H . The solid red lines indicate the best fit for the observed dispersion, being a combination of both peculiar velocity errors and a constant variance for each filter.

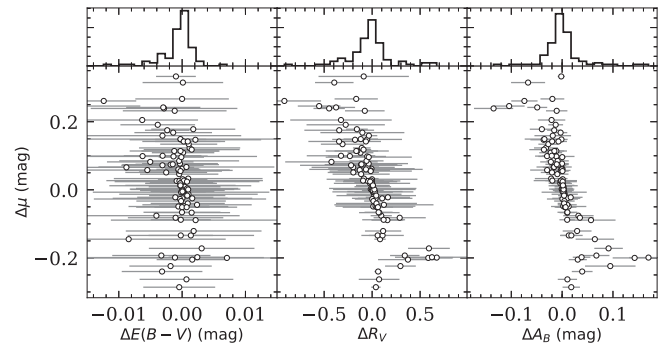


Figure 6. Comparison between the distance residuals $\Delta\mu$ and the difference between the best-fit values of color excess (left panel), reddening coefficient (middle panel), and total absorption in the B band (right panel). The horizontal error bars represent the width of the prior that was used when calibrating the luminosity–decline rate relation. The top panels show histograms of the changes in each of the extinction parameters to help show that the distributions are not biased.

well-understood systematics (Madore & Freedman 1991; Sandage & Tammann 2006; Freedman & Madore 2010). Their disadvantage is that at the distance of the closest SNe Ia, the typical angular separations of stars in the host are small enough to require space-based observations. Even with the *Hubble Space Telescope*, though, there is significant crowding and overlapping of point-spread functions, requiring corrections that can approach the flux level of the Cepheid itself (Riess et al. 2011).

A promising alternative to Cepheids is the Tip of the Red Giant Branch (TRGB) method (Madore et al. 2009; Jang et al. 2017). A significant advantage with TRGB is that the older stellar populations being considered are found in both early- and late-type galaxies, allowing for potentially more nearby calibrating SN Ia hosts. The method is also typically carried out in the outskirts of the hosts, reducing the crowding significantly. The Carnegie-Chicago Hubble Program (CCHP; Beaton et al. 2016; W. F. Freedman 2018, in preparation) aims to measure H_0 using population II distance indicators, and the CSP-I and CSP-II samples will be a significant component of their work.

For the purposes of this paper, we will forgo using the existing TRGB sample as it is rather sparse and lacks SNe Ia that were observed in the NIR. We therefore use the Cepheid sample of Riess et al. (2016) to calibrate our Hubble diagram as it is the most comprehensive data set under a single photometric system. In the following sections, we present the general method, and then consider different data subsamples and their effects on the derived value of H_0 .

5.1. Cepheid Distances

Table 4 lists the SNe Ia we consider with Cepheid distances from Riess et al. (2016), their hosts, and the source of the optical and NIR photometry. A significant number (15/19) have SNe Ia whose brightness was measured in the NIR and can be used to improve the estimates of reddening and the slope of the reddening law (see Section 4.2). There are also five SNe Ia that were observed by the CSP and for which there will be no systematic errors due to differences in photometric calibration.

The models we wish to fit are the same as Equations (4) and (7), except that now we allow H_0 to vary. This will result in a degeneracy with the zeroth-order term of $P_\lambda^N(s_{BV} - 1)$, so we need SNe Ia whose distances are independent of H_0 . We

Table 4
Cepheid Hosts Used to Anchor Type Ia SN Distance Scale

SN	Host	Opt. Ref.	NIR Ref.	Comments	μ (mag) mag
1981B	NGC 4536	Buta & Turner (1983)	Elias et al. (1981)	NIR	30.89(06)
1990N	NGC 4639	Leibundgut et al. (1991)	31.49(08)
1994ae	NGC 3370	Riess et al. (2005)	32.05(06)
1995al	NGC 3021	Riess et al. (1999)	32.48(10)
1998aq	NGC 3982	Riess et al. (2005)	31.72(08)
2001el	NGC 1448	Krisciunas et al. (2003)	Krisciunas et al. (2003)	NIR	31.28(06)
2002fk	NGC 1309	Silverman et al. (2012)	Cartier et al. (2014)	NIR	32.49(07)
2003du	U9391	Hicken et al. (2009)	Stanishev et al. (2007)	NIR	32.88(07)
2005cf	NGC 5917	Wang et al. (2009)	Friedman et al. (2015)	NIR	32.25(11)
2007af	NGC 5584	Stritzinger et al. (2011)	Stritzinger et al. (2011)	NIR, CSP-I	31.75(06)
2007 sr	NGC 4038	Schweizer et al. (2008)	Schweizer et al. (2008)	NIR, CSP-I	31.28(13)
2009ig	NGC 1015	Hicken et al. (2012)	Friedman et al. (2015)	NIR	32.47(10)
2011fe	NGC 5457	Richmond & Smith (2012)	Matheson et al. (2012)	NIR	29.16(05)
2011by	NGC 3972	Silverman et al. (2013)	Friedman et al. (2015)	NIR	31.60(08)
2012cg	NGC 4424	Marion et al. (2016)	Marion et al. (2016)	NIR	31.08(32)
2012fr	NGC 1365	Contreras et al. (2018)	Contreras et al. (2018)	NIR, CSP-I	31.29(07)
2012ht	NGC 3447	This work	This work	NIR, CSP-II	31.88(05)
2013dy	NGC 7250	Pan et al. (2015)	Pan et al. (2015)	NIR	31.47(09)
2015F	NGC 2442	This work	This work	NIR, CSP-II	31.56(07)

therefore modify the distance moduli from Equations (4) and (7) to be as follows:

$$\mu = \begin{cases} \mu_{\text{ceph},i} & i \in \{\text{Cepheid hosts}\} \\ \mu(z_{\text{hel}}, z_{\text{cmb}}, H_0, q_0) & \text{otherwise.} \end{cases} \quad (8)$$

Here, $\mu_{\text{ceph},i}$ is the distance modulus of the galaxy in the set {Cepheid hosts} hosting the SN Ia, and we use the standard second-order expansion of the luminosity distance for the rest:

$$\begin{aligned} & \mu(z_{\text{hel}}, z_{\text{cmb}}, H_0, q_0) \\ &= 5 \log_{10} \left[\left(\frac{1 + z_{\text{hel}}}{1 + z_{\text{cmb}}} \right) \frac{cz_{\text{cmb}}}{H_0} \left(1 + \frac{1 - q_0}{2} z_{\text{cmb}} \right) \right] + 25 \end{aligned} \quad (9)$$

is the distance modulus from the Hubble law with cosmic deceleration $q_0 = \Omega_m/2 - \Omega_\Lambda = -0.53$ (Planck Collaboration et al. 2016). The factor $(1 + z_{\text{hel}})/(1 + z_{\text{cmb}})$ accounts for the fact that observational effects such as time dilation should be corrected using redshift relative to the heliocentric frame of reference, z_{hel} , whereas cosmological distances should be computed using redshift relative to the cosmic microwave background (CMB), z_{CMB} .

The key to solving for H_0 therefore lies entirely in the determination of the distances to the calibrating hosts $\mu_{\text{ceph},i}$. These are determined using the Leavitt period–luminosity law with linear corrections based on the color of the Cepheid and its metallicity (Freedman & Madore 2011; Riess et al. 2016). This is implemented in the following model for the observed magnitudes of the Riess et al. (2016) sample of Cepheid variables:

$$\begin{aligned} m_H^{\text{Ceph}} &= M_H^{\text{Ceph}} + \mu_{\text{ceph},i} + \alpha \log_{10} P + \beta(V - I) \\ &+ \gamma [\text{O}/\text{H}]. \end{aligned} \quad (10)$$

Here, M_H^{Ceph} and α are the zero-point and slope of the Leavitt law, P is the period of the Cepheid, β is the slope of the Wesenheit correction using $V - I$ color, and γ is the correction factor for the effect of the metallicity $[\text{O}/\text{H}]$ (Freedman & Madore 2011).

Now we are left with a degeneracy between M^{Ceph} and the distance moduli to the hosts μ_i , which we break by calibrating the Cepheids themselves using fundamental distance indicators to the Large Magellanic Cloud (LMC), the water maser galaxy NGC 4258, and galactic Cepheids with parallax measurements. We model these as follows:

$$\begin{aligned} m_H^{\text{Ceph}}(\text{LMC}) &= M_H^{\text{Ceph}} + \mu_{\text{LMC}} + \alpha \log_{10} P \\ &+ \beta(V - I) + \gamma [\text{O}/\text{H}]_{\text{LMC}} + \epsilon_{\text{zp,LMC}}, \\ m_H^{\text{Ceph}}(\text{N4258}) &= M_H^{\text{Ceph}} + \mu_{\text{N4258}} + \alpha \log_{10} P \\ &+ \beta(V - I) + \gamma [\text{O}/\text{H}], \\ m_H^{\text{Ceph}}(\text{MW}) &= M_H^{\text{Ceph}} - 5 \log_{10} \pi - 5 + \alpha \log_{10} P \\ &+ \beta(V - I) + \gamma [\text{O}/\text{H}] + \epsilon_{\text{zp,MW}}, \end{aligned} \quad (11)$$

where $\mu_{\text{LMC}} = 18.49 \pm 0.05$ mag (Riess et al. 2016) and $\mu_{\text{N4258}} = 29.40 \pm 0.23$ mag (Humphreys et al. 2013) are assigned Gaussian priors, and the 10 Milky Way parallaxes π are given by Benedict et al. (2007). We include possible systematic offsets $\epsilon_{\text{zp,LMC}}$ and $\epsilon_{\text{zp,MW}}$ between the *F104W* system used by Riess et al. (2016) and those used by Persson et al. (2004) for the LMC Cepheids as well as the local Milky Way Cepheids (Groenewegen 1999). Furthermore, we include similar terms for the possible systematic offsets between the CSP-I natural system and the photometric systems listed in Table 4. Since these are completely unknown, we place a Gaussian prior on each centered at zero and with a width equal to the error in the zero-point for each filter (see Appendix D). At this point, we do not use known Cepheids from the DR2 release of *Gaia*, as they are all bright, and there appears to be a zero-point offset in the absolute parallaxes that is dependent on the brightness of the star (Lindgren et al. 2018). The systematic uncertainty in this offset could be as high as 0.02 mas (Riess et al. 2018), resulting in a systematic distance error of approximately 7%. Using *Gaia* as a robust anchor will have

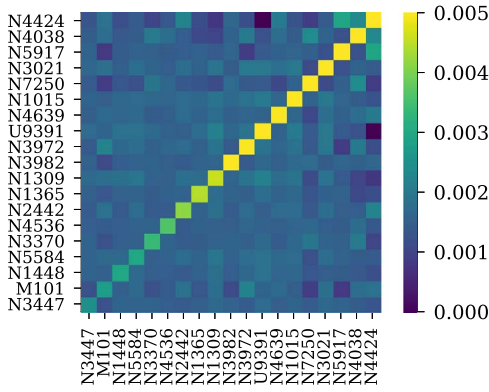


Figure 7. Visualization of the covariance matrix for the calibrating host galaxies of SNe Ia. Each off-diagonal pixel represents the covariance between two host galaxies, while the diagonal represents the variance of a single host. The rows and columns have been sorted by increasing variance. The levels have been clipped to the interval (0, 0.005) in order to better visualize the off-diagonal values.

to await the classification and subsequent photometric follow-up of fainter Cepheids.

When including the Riess et al. (2016) Cepheid data, one must be very careful of the statistical description of the photometry. Working in flux units with properly weighted distributions, as we do with the SN photometry, is not possible, due to unknown bias corrections and sigma clipping that have been performed on the Riess et al. (2016) data. Since the authors have not published these corrections, one is forced to work in magnitudes. For more details, see Appendix E.

Since the link between the Cepheid sample and the SN Ia sample is the set of distance moduli for the calibrating hosts, $\mu_{\text{ceph},i}$, we can split the MCMC simulation into two steps: (1) determine the values $\mu_{\text{ceph},i}$ for the calibrating hosts, including a complete covariance matrix $C(\mu)$, and (2) use these as priors for the SN Ia MCMC runs. This allows for a much more efficient use of computing time, as one can experiment with how the supernova properties and priors affect H_0 without having to recompute the Cepheid calibration. We have published our covariance matrices $C(\mu)$ as part of the online data, and they can be used by anyone who wishes to use the host distances consistently without having to deal with the Cepheid data itself. The software is also available to fit with different priors and probability models. A sample covariance matrix is shown in Figure 7 and shows the large range of uncertainty in the Cepheid host distances. To better visualize the off-diagonal values, we have clipped the color map to a maximum of $\sigma^2 = 0.005$. The true extent of the diagonal elements is from an error of ± 0.05 mag (NGC 3447) to ± 0.32 mag (NGC 4424). There is very little structure in the off-diagonal terms, indicating that the primary source of covariance is the systematic error in the distances to the fundamental anchors (LMC, NGC 4258, and MW Cepheids).

5.2. Results

Many previous analyses have investigated numerous systematic effects related to the Cepheid sample, including the effects of omitting objects based on period and metallicity, as well as the inclusion or exclusion of the fundamental anchors (e.g., Riess et al. 2016). Rather than run our simulations on various subsamples of the Cepheid data (e.g., cut out low/high-period Cepheids, include/exclude LMC, MW, and NGC 4258),

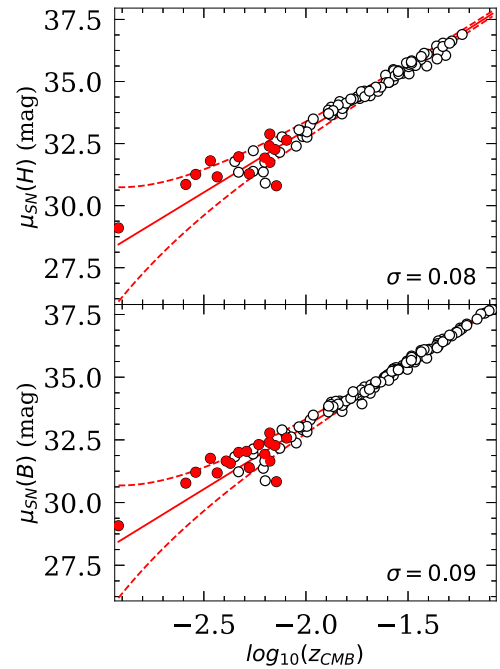


Figure 8. Hubble diagram for the H band (top panel) and B band (bottom panel) populated with SNe Ia from the CSP-I DR3 sample, as well as with those objects with Cepheid hosts (plotted as solid red circles). The best-fit $H_0 = 73.5 \pm 1.5 \text{ km s}^{-1} \text{ Mpc}^{-1}$ from combining all filters is shown by a solid red line. The expected dispersion due to intrinsic variance and peculiar velocities is plotted as dashed red lines.

we use all of the available data and do our best to model the residuals through several nuisance parameters such as $\epsilon_{zp,i}$ and intrinsic dispersions and restricting the limits of predictor variables such as period. In this way, we include these important systematic errors without having to run multiple scenarios with different Cepheid subsamples, instead focusing on the systematics related to the SNe Ia. The full details of the Bayesian model and associated priors that were used can be found in Appendix E.

Figure 8 shows the Hubble diagram for two bands, B and H , using the extinction-based color corrections. The best-fit value of the Hubble constant H_0 is shown as solid red lines, and the predicted dispersions due to peculiar velocities and intrinsic widths of the luminosity–decline rate relation (labeled) are shown as dashed red lines. The red points correspond to the SNe in hosts with Cepheid distances.

Table 5 lists a summary of the values of H_0 derived when using the two different methods of dealing with the host galaxy extinction for each of the CSP-I filters. We also split our SNe Ia into several subsamples, as we did in Sections 4.1 and 4.3. We provide three uncertainties in H_0 : (1) the uncertainty σ_{SN} when the distances to the Cepheid hosts are kept fixed, (2) the uncertainty σ_{total} when all parameters are allowed to vary, and (3) the uncertainty $\sigma_{\text{Ceph}} = \sqrt{\sigma_{\text{tot}}^2 - \sigma_{\text{SN}}^2}$. This separation should give an indication of the error budget due to the supernova and Cepheid data. The final column indicates the number of SNe Ia observed in each filter that have Cepheid distances. The systematics involved with the Cepheids are well known and will not be discussed further here. We turn instead to discussion of the SN-related effects.

The largest source of systematic error for our SN sample is the difference in average host galaxy stellar mass between the Cepheid sample and the more distant sample. The limited mass

Table 5
Best-fit Values of H_0 in $\text{km s}^{-1} \text{Mpc}^{-1}$

Filters	Tripp				$E(B - V)$				N_{calib}
	H_0	σ_{Ceph}	σ_{SN}	σ_{total}	H_0	σ_{Ceph}	σ_{SN}	σ_{total}	
Full Sample									
u	73.98	1.53	3.10	3.45	74.02	1.27	2.90	3.17	11
B	72.74	1.38	1.60	2.11	72.39	1.33	1.69	2.15	19
V	72.64	1.38	1.57	2.09	72.80	1.25	1.60	2.03	19
g	74.32	1.59	2.45	2.92	75.90	1.54	2.87	3.26	5
r	71.85	1.36	1.48	2.01	71.86	1.23	1.61	2.02	18
i	72.98	1.32	1.54	2.03	73.01	1.32	1.73	2.18	18
Y	72.25	1.22	2.35	2.65	74.28	1.48	3.13	3.46	6
J	72.47	1.24	1.74	2.14	73.11	1.38	2.01	2.44	15
H	73.86	1.24	1.78	2.17	74.54	1.26	2.08	2.43	15
$s_{BV} > 0.5$									
u	73.75	1.56	3.05	3.43	73.37	1.39	2.77	3.10	11
B	72.44	1.37	1.60	2.10	71.79	1.23	1.68	2.08	19
V	72.42	1.38	1.58	2.10	72.33	1.20	1.60	2.00	19
g	74.10	1.63	2.42	2.92	75.28	1.36	2.66	2.99	5
r	71.61	1.38	1.49	2.03	71.50	1.24	1.59	2.02	18
i	72.78	1.30	1.55	2.02	72.73	1.33	1.75	2.20	18
Y	71.82	1.23	2.26	2.58	74.12	1.57	3.09	3.47	6
J	71.75	1.20	1.68	2.06	72.37	1.21	2.02	2.35	15
H	72.98	1.17	1.77	2.12	73.85	1.13	2.12	2.40	15
$E(B - V) < 0.5$									
u	73.95	1.55	2.98	3.36	73.69	1.17	2.95	3.18	11
B	72.60	1.40	1.57	2.10	71.90	1.18	1.57	1.96	19
V	72.51	1.36	1.59	2.09	72.30	1.25	1.45	1.91	19
g	74.18	1.54	2.41	2.86	75.36	1.47	2.46	2.86	5
r	71.69	1.38	1.47	2.02	71.47	1.27	1.47	1.94	18
i	72.79	1.35	1.56	2.06	72.56	1.31	1.68	2.13	18
Y	72.01	1.22	2.27	2.57	73.33	1.34	2.67	2.99	6
J	71.80	1.23	1.71	2.11	72.50	1.35	1.84	2.29	15
H	73.16	1.21	1.77	2.14	74.10	1.16	1.99	2.31	15
$s_{BV} > 0.5$ and $E(B - V) < 0.5$									
u	73.99	1.60	2.98	3.38	72.93	1.33	2.77	3.07	11
B	72.67	1.39	1.56	2.09	71.19	1.18	1.52	1.92	19
V	72.52	1.36	1.57	2.07	71.70	1.20	1.45	1.88	19
g	74.11	1.57	2.42	2.89	74.67	1.38	2.19	2.59	5
r	71.73	1.38	1.50	2.03	71.03	1.21	1.48	1.91	18
i	72.77	1.36	1.57	2.07	72.16	1.32	1.67	2.12	18
Y	71.87	1.25	2.22	2.54	72.94	1.40	2.63	2.98	6
J	71.78	1.32	1.70	2.15	71.74	1.25	1.82	2.21	15
H	73.00	1.18	1.77	2.13	73.23	1.08	1.99	2.26	15

range of the CSP-I sample not only introduces a covariance between the H_0 and α_M , it also limits the precision of our estimates for α_M , thereby increasing the overall systematic error in H_0 . In principle, we could use the value of α_M determined from other samples as a prior, but we would be limited to the *B* band, and we prefer to implement an independent measure of the host mass effect. The increased range in host mass in the CSP-II sample will greatly alleviate this systematic.

In general, the uncertainties in H_0 measured using the extinction method are larger than that found by the Tripp method. This is because, in the Tripp method, there is a single reddening “slope” whose uncertainty is reduced as \sqrt{N} , whereas in the extinction method, it is assumed there is an underlying distribution of R_V whose width does not decrease with SN sample size. We believe this more faithfully describes the observed diversity in reddening properties of SN Ia hosts and should be included in the error budget.

A major goal of the CSP-I was to provide a Hubble constant entirely based on NIR data (both for the Cepheids and SNe).

We provide such estimates for all three NIR bands, though clearly the *Y* band’s constraint is weaker because it only has five calibrating SNe (the same is true for the *g* band). Bands *J* and *H* have fewer calibrating SNe than the optical filters, but have comparable uncertainties, which is partly due to their decreased sensitivity to both the reddening and host-galaxy mass corrections (see Tables 1 and 3). In particular, the *H* band has the lowest host mass dependence $\alpha_M = -0.04 \pm 0.03$ and lowest extinction dependence, and it is nearly consistent with no color-stretch dependence. We therefore take the *H*-band determination of $H_0 = 73.2 \pm 2.3 \text{ km s}^{-1} \text{Mpc}^{-1}$ as our best estimate, a value nearly identical to that obtained by Riess et al. (2016) using SNe Ia in optical wavelengths with a Tripp correction. Our value using Tripp and the *B* band yields $H_0 = 72.67 \pm 2.1 \text{ km s}^{-1} \text{Mpc}^{-1}$, somewhat lower but well within uncertainties. It is also consistent with a previous NIR determination of the Hubble constant by Dhawan et al. (2018), who found $H_0 = 72.8 \pm 3.1 \text{ km s}^{-1} \text{Mpc}^{-1}$ and used CSP-I photometry as part of their sample.

In general, our bluer wavelengths yield estimates of H_0 that are systematically lower, but we caution that at these wavelengths, the host galaxy mass corrections are larger, which, due to the difference in average stellar mass between the distant and Cepheid hosts, leads to a lower value for H_0 . Future estimates based on CSP-II objects, which span a more representative range of host masses, will make these estimates more reliable.

6. Conclusions

In this paper, we have presented an updated calibration of the CSP-I sample of SNe Ia using a variety of methods and assumptions and the resulting values for the Hubble constant H_0 . The calibrations are most useful for the astronomical community to determine distances and extinctions to SNe Ia outside the CSP-I sample in order constrain host-galaxy properties or analyze the physics of the SNe Ia themselves.

In the forefront of our analysis is the introduction of a new light-curve shape parameter, s_{BV} , that we feel is a more reliable measure of the decline rate of SNe Ia than $\Delta m_{15}(B)$. The reason for this is that s_{BV} measures the temporal location of a very specific and physically well-understood transition in the ejecta: the recombination of Fe III \rightarrow Fe II. This in turn depends on the temperature evolution of the ejecta and hence the overall energy budget. In contrast, $\Delta m_{15}(B)$ depends much more on the details of the energy transport through the ejecta, and for the fast decliners, the transition from optically thick to thin occurs near or before day 15, leading to a breakdown in the ability of $\Delta m_{15}(B)$ to classify these objects. Ultimately, the validation of s_{BV} as a light-curve parameter will require more fast-declining objects in the Hubble flow. This is hampered by the fact that the fast decliners are also subluminal compared to “normal” SNe Ia. Alternatively, finding fast-declining objects in galaxies that have redshift-independent distances, including those that have hosted other normal SNe Ia, can also allow us to verify how precise their distances can be estimated. This is the case with SN 2006mr, our fastest-declining object. Using the mean distance from three other SNe Ia, we find that the distance inferred from SN 2006mr is consistent to within the uncertainties from the luminosity–decline rate relation. The ability of a single light-curve parameter to predict both the intrinsic color and luminosity of SNe Ia over such a large range of decline rates suggests that there is a single explosion mechanism at work.

A great deal of effort has been done to accurately measure the intrinsic colors and extinctions of our sample. This allows us to not only produce absolute luminosities for our objects, but also deal with the fact that the value of R_V is highly variable. In the case where the extinction is high, the colors tell us what R_V is and give a more reliable extinction correction. In the case where extinction is low, the value of R_V is inherited from the mean of the training sample, but so is its underlying variance, yielding a more reliable error in the extinction correction. We have used these extinction estimates to produce as accurate an estimate as possible for the extinction-corrected absolute magnitudes using photometric data on a single well-understood system. This will be invaluable to the theoretical community for testing explosion models (Kasen & Woosley 2007; Hsiao et al. 2013; Stritzinger et al. 2015; Hoefflich et al. 2017).

Finally, we have derived several estimates for the value of H_0 using two different approaches to the color correction, multiple wavelengths, and different subsamples. Unsurprisingly, we find that the differences are greatest when the average properties (decline rate, color, and host mass) of the calibrating SNe Ia differ from the distant sample. In the case of decline rate and color, the more extreme cases in the distant sample are rare and can be eliminated from the sample without increasing the final error budget in H_0 . This is not the case for host galaxy mass, where the calibrating sample hosts are significantly lower in mass than the majority of the distant hosts. This is simply a result of sampling the Cepheid hosts from a smaller volume and relying on targeted searches for the distant sample. Here, the H band clearly has an advantage that is due to its relative insensitivity to host galaxy mass.

The use of NIR data to constrain cosmology therefore continues to show promise. Aside from the fact that the NIR allows one to more accurately constrain the extinction of the SNe Ia, its relative insensitivity to variations in the reddening law R_V generally yields tighter constraints on H_0 despite having fewer Cepheid hosts. The disadvantages of the NIR are the relative faintness of the SNe and the brightness of the background sky, requiring more observational resources than in the optical. There is also more uncertainty in the filter responses and zero-points due to atmospheric effects (see Appendix D), which is particularly worrisome for a high- z cosmology, where cross-band K-corrections are required. Progress can be made here by moving to space-based observations or improving our atmospheric monitoring and corrections, particularly with regard to precipitable water vapor.

Our use of NIR data to constrain cosmology will also improve with an increased sample of objects farther out in the Hubble flow. At present, the CSP’s sample of objects has a median redshift of $z \sim 0.025$ and is biased to high-luminosity hosts. The CSP-II, which has now finished observations, will provide approximately 120 SNe Ia with a median redshift of $z \sim 0.056$ drawn from untargeted surveys. This will allow us to more accurately determine the intrinsic dispersion of SNe Ia and possible correlations with host galaxy properties in the NIR.

We are also collaborating with the Carnegie Hubble Program (Freedman et al. 2011), which seeks to establish a mid-infrared distance ladder from the Milky Way all the way out to the hosts of SNe Ia using Cepheids, providing a completely independent anchor. The CSP-II will be able to provide the final rung of this distance ladder in the NIR out to $z \sim 0.1$.

We thank the anonymous referee for carefully reviewing this paper and helping to improve its clarity. We also thank Adam Riess and Dan Scolnic for their help in better understanding the SH0ES Cepheid data. The work of the CSP has been supported by the National Science Foundation under grants AST0306969, AST0607438, AST1008343, AST1613426, and AST1613472. M.D.S. acknowledges support from the Danish Agency for Science and Technology and Innovation through a Sapere Aude Level 2 grant and funding by a research grant (13261) from VILLUM FONDEN. N.S. acknowledges the financial support of the George P. and Cynthia Wood Mitchell Institute for Fundamental Physics and Astronomy. This paper includes data gathered with the 6.5 m *Magellan* Telescopes located at Las Campanas Observatory, Chile. Computing resources used

for this work were made possible by a grant from the Ahmanson Foundation. We thank the Cynthia and George Mitchell Foundation and Sheridan Lorenz for their support of a number of CSP workshops held at the Cook’s Branch Nature Conservancy, where some of this work was done. This research has made use of the NASA/IPAC Extragalactic Database (NED), which is operated by the Jet Propulsion Laboratory, California Institute of Technology, under contract with the National Aeronautics and Space Administration.

Appendix A Photometry of SN 2012ht and SN 2015F

In Section 5 we used two SNe Ia from the CSP-II project to anchor the SN Ia distance ladder, so we present their photometry in this section. The CSP-II is a continuation of CSP-I, with a particular emphasis on the NIR observations at higher redshift than in the CSP-I. The observational setup and procedure in the optical are identical to CSP-I, and details are given by Krisciunas et al. (2017). For the NIR observations, we moved RetroCam from the Swope telescope to the du Pont at LCO. Other than that, our observational procedures and data reduction are identical to the CSP-I, and the complete telescope, filter, and CCD transmission functions have been measured, which are available at the CSP website.¹² Note that, in 2013 October, the CCD detector on the Swope telescope was upgraded from a Site3 to e2v CCD. This resulted in a change to our filter functions and zero-points in the optical. SN 2012ht is therefore on the old CSP-I natural system, whereas SN 2015F is on the new one. Both SNe are on the new du Pont RetroCam natural system, which is described in Contreras et al. (2018).

Table 6 lists the photometry of SN 2012ht and SN 2015F. Tables 7 and 8 list the photometry of the reference stars in the standard optical (Landolt 1992; Smith et al. 2002) and NIR

Table 6
Photometry of CSP SNe Ia in Cepheid Hosts

MJD (days)	Filter	Mag	Phase (days)
SN 2012ht			
56282.3	<i>B</i>	15.737(0.035)	−13.4
56283.3	<i>B</i>	15.258(0.037)	−12.4
56285.3	<i>B</i>	14.405(0.035)	−10.4
56286.3	<i>B</i>	14.093(0.036)	−9.4
56289.3	<i>B</i>	13.501(0.040)	−6.4
56290.3	<i>B</i>	13.382(0.037)	−5.4
56291.3	<i>B</i>	13.277(0.037)	−4.4
56292.3	<i>B</i>	13.210(0.039)	−3.4
56295.3	<i>B</i>	13.111(0.035)	−0.4
...
SN 2015F			
57092.1	<i>B</i>	16.939(0.011)	−14.8
57093.1	<i>B</i>	16.253(0.009)	−13.8
57094.0	<i>B</i>	15.704(0.013)	−12.9
57095.1	<i>B</i>	15.209(0.013)	−11.8
57096.0	<i>B</i>	14.829(0.011)	−10.9
57097.1	<i>B</i>	14.510(0.010)	−9.8
57098.1	<i>B</i>	14.254(0.008)	−8.8
57099.0	<i>B</i>	14.076(0.012)	−7.9
57100.1	<i>B</i>	13.895(0.011)	−6.8
57101.0	<i>B</i>	13.739(0.006)	−5.9
57102.1	<i>B</i>	13.637(0.006)	−4.8

(This table is available in its entirety in machine-readable form.)

(Persson et al. 1998) systems. The filter functions and photometric zero-points zp_λ of the CSP-I and CSP-II natural systems are available at the CSP website. These can be used to S-correct (Stritzinger et al. 2005) the photometry to other systems (see Appendix D).

¹² <https://csp.obs.carnegiescience.edu>

Table 7
Optical Photometry of Secondary Standards in the Standard Systems of Smith et al. (2002) and Landolt (1992)

ID	α (2000)	δ (2000)	u'	g'	r'	i'	B	V
SN 2012ht								
1	10:53:39.48	+16:49:16.9	16.832(044)	15.574(025)	15.128(019)	14.973(021)	15.939(031)	15.309(023)
2	10:53:36.34	+16:49:54.0	18.770(109)	16.509(043)	15.617(028)	15.276(028)	17.038(054)	16.015(034)
3	10:53:30.02	+16:50:26.4	18.373(107)	17.227(056)	16.883(046)	16.751(074)	17.514(091)	17.008(085)
4	10:53:18.67	+16:49:20.4	17.961(055)	16.478(036)	15.929(031)	15.746(032)	16.892(051)	16.147(056)
6	10:53:23.78	+16:48:15.0	...	17.748(115)	17.046(078)	16.762(073)	18.212(110)	17.356(093)
7	10:53:14.61	+16:45:51.6	...	19.331(099)	18.205(091)	17.722(101)	0.000(000)	18.586(083)
8	10:53:12.91	+16:45:20.7	...	17.501(062)	16.104(031)	14.620(021)	18.337(136)	16.684(062)
10	10:53:19.68	+16:43:29.5	19.046(037)	18.015(117)	17.544(054)	17.331(108)	18.304(111)	17.692(087)
11	10:53:15.43	+16:42:48.5	18.835(081)	16.819(066)	15.479(015)	14.696(017)	17.592(100)	16.084(063)
12	10:53:10.80	+16:43:24.2	14.540(017)	13.371(014)	12.991(010)	12.874(011)	13.693(014)	13.139(014)
13	10:53:35.45	+16:42:25.3	18.381(058)	17.099(058)	16.563(045)	16.376(060)	17.465(094)	16.731(042)
SN 2015F								
2	07:35:55.06	−69:24:58.4	15.225(005)	13.645(003)	13.056(006)	12.863(006)	14.046(011)	13.301(003)
3	07:35:57.21	−69:27:12.0	15.181(005)	13.864(003)	13.373(004)	13.196(005)	14.212(011)	13.575(003)
4	07:35:13.04	−69:29:57.7	15.870(005)	14.280(003)	13.612(003)	13.333(004)	14.709(012)	13.903(003)
5	07:35:02.17	−69:23:12.0	16.885(008)	14.492(003)	13.532(004)	13.134(023)	15.081(014)	13.953(003)
6	07:36:01.21	−69:37:45.1	15.753(006)	14.358(003)	13.823(003)	13.621(003)	14.729(010)	14.051(004)
7	07:36:57.82	−69:36:11.5	16.231(005)	14.570(003)	13.876(002)	13.603(003)	15.017(012)	14.184(003)
8	07:35:32.74	−69:34:20.3	15.969(005)	14.594(003)	14.048(002)	13.834(003)	14.967(011)	14.278(003)
9	07:37:27.92	−69:26:45.3	16.142(005)	14.668(003)	14.118(002)	13.924(002)	15.057(013)	14.353(003)
10	07:34:59.88	−69:35:36.1	17.677(010)	14.996(003)	13.944(002)	13.488(003)	15.610(017)	14.418(003)
11	07:37:26.81	−69:27:13.5	16.503(006)	14.819(003)	14.174(002)	13.942(002)	15.254(009)	14.452(003)
12	07:35:13.96	−69:23:25.6	16.250(005)	14.833(003)	14.253(002)	14.023(002)	15.212(016)	14.496(003)
13	07:35:54.32	−69:24:19.3	16.882(007)	14.997(003)	14.218(002)	13.916(002)	15.485(023)	14.552(003)
14	07:37:09.56	−69:26:09.1	16.201(005)	14.938(003)	14.472(002)	14.291(002)	15.275(013)	14.667(003)
15	07:35:06.59	−69:35:23.9	16.842(007)	15.082(003)	14.379(002)	14.094(002)	15.534(017)	14.685(003)
16	07:36:26.34	−69:26:17.8	16.293(006)	15.045(003)	14.574(002)	14.399(002)	15.380(016)	14.770(003)
17	07:37:21.60	−69:26:51.5	16.593(006)	15.138(003)	14.577(002)	14.361(002)	15.535(010)	14.817(003)
18	07:36:31.03	−69:29:30.6	16.707(006)	15.225(003)	14.563(002)	14.287(002)	15.641(019)	14.860(003)
19	07:36:23.37	−69:23:58.9	17.164(008)	15.367(003)	14.637(002)	14.354(002)	15.828(027)	14.953(003)
20	07:36:31.45	−69:37:16.7	16.816(007)	15.330(003)	14.730(003)	14.497(002)	15.736(014)	14.989(003)
21	07:37:24.84	−69:30:31.9	16.719(006)	15.345(003)	14.763(003)	14.524(002)	15.728(016)	15.016(003)
22	07:37:02.86	−69:32:36.1	17.664(010)	15.516(003)	14.694(003)	14.399(002)	16.018(020)	15.062(003)
23	07:35:37.73	−69:27:52.9	17.065(007)	15.545(003)	14.910(003)	14.684(002)	15.947(022)	15.177(003)
24	07:36:48.87	−69:26:04.5	16.864(007)	15.553(003)	15.027(003)	14.824(002)	15.913(024)	15.252(003)
25	07:37:15.38	−69:26:48.0	16.876(007)	15.565(003)	15.063(003)	14.880(002)	15.925(018)	15.273(003)
26	07:35:07.75	−69:23:12.9	16.883(008)	15.376(003)	14.741(003)	14.495(003)	15.776(022)	15.009(003)
27	07:36:47.77	−69:35:48.1	17.222(008)	15.769(003)	15.145(003)	14.900(002)	16.186(022)	15.411(003)
28	07:35:44.55	−69:36:21.2	17.429(009)	15.824(003)	15.121(003)	14.826(003)	16.256(025)	15.435(003)
29	07:36:34.68	−69:29:35.7	18.523(019)	16.037(003)	14.978(003)	14.564(002)	16.589(024)	15.481(003)
30	07:36:41.69	−69:24:00.0	17.420(009)	15.915(003)	15.289(003)	15.024(003)	16.323(028)	15.562(003)
31	07:37:07.50	−69:33:46.2	17.587(010)	15.964(003)	15.336(003)	15.113(003)	16.396(022)	15.605(003)

(This table is available in machine-readable form.)

Table 8
NIR Photometry of Secondary Standards

ID	α (2000)	δ (2000)	Y	J	H
SN 2012ht					
101	10:53:23.91	+16:46:38.9	15.088(030)	14.608(021)	13.954(045)
102	10:53:21.20	+16:48:00.0	15.601(039)	15.149(011)	14.556(037)
103	10:53:23.81	+16:48:14.9	15.922(026)	15.627(027)	15.114(013)
104	10:53:28.19	+16:46:49.9	16.512(087)	16.256(095)	15.501(041)
105	10:53:17.48	+16:45:05.1	16.807(062)	16.371(012)	15.841(084)
106	10:53:15.49	+16:46:55.3	16.989(054)	16.407(031)	15.902(063)
107	10:53:21.01	+16:45:22.0	17.919(103)	17.414(055)	16.884(194)
SN 2015F					
101	07:36:31.00	−69:29:31.1	13.494(024)	13.162(023)	12.723(028)
102	07:36:34.61	−69:29:36.3	13.636(026)	13.239(027)	12.645(039)
103	07:36:07.16	−69:28:51.8	14.796(047)	14.449(062)	14.052(069)
104	07:36:31.16	−69:29:59.5	15.158(044)	14.898(038)	14.557(060)
106	07:36:17.75	−69:28:28.8	15.755(048)	15.236(042)	14.605(139)
107	07:36:22.93	−69:30:25.6	15.652(063)	15.264(044)	14.759(045)
108	07:36:18.43	−69:28:59.9	16.110(059)	15.713(052)	15.139(066)
109	07:36:15.17	−69:29:36.7	16.709(055)	16.232(085)	15.575(143)
110	07:36:22.02	−69:28:50.5	16.798(097)	16.344(120)	15.773(132)
111	07:36:32.03	−69:28:59.4	16.822(067)	16.531(155)	16.103(128)
112	07:36:01.57	−69:30:57.5	16.951(054)	16.563(159)	15.736(269)
113	07:36:36.41	−69:29:10.4	0.000(000)	16.432(079)	16.066(076)
114	07:36:08.92	−69:30:22.5	16.924(128)	16.475(124)	15.715(222)
115	07:36:13.37	−69:29:41.5	17.362(088)	16.890(130)	16.324(106)
116	07:36:02.64	−69:28:41.1	17.375(093)	16.758(089)	15.867(090)
117	07:36:36.42	−69:29:56.9	0.000(000)	16.432(081)	16.576(195)
118	07:36:20.70	−69:30:09.5	17.462(097)	17.037(132)	...
119	07:36:01.19	−69:29:02.9	17.358(408)	16.865(420)	15.706(103)
120	07:36:22.39	−69:31:12.2	17.313(141)	16.722(132)	15.912(126)
121	07:36:33.40	−69:29:07.7	17.639(091)	17.031(123)	16.429(101)
122	07:36:06.88	−69:30:25.3	17.253(025)	16.767(050)	15.952(097)
123	07:36:29.68	−69:29:22.3	...	17.232(130)	16.345(090)

(This table is available in machine-readable form.)

Appendix B

Host Galaxy Mass

In recent years, there has been evidence of a correlation between the color- and decline rate-corrected luminosity of SNe Ia and bulk properties of their host galaxies. For nearby SNe Ia, Neill et al. (2009) found a correlation between host age and corrected peak brightness, and Kelly et al. (2010) found a 2.5σ correlation between host galaxy stellar mass and corrected peak brightness, both using a sample similar to the CSP-I sample. Using a more distant sample from the Supernova Legacy Survey (SNLS), Sullivan et al. (2010) show a similar trend with stellar mass, measuring a nonzero gradient at $\sim 3\sigma$. More recently, Uddin et al. (2017) have used a comprehensive set of more than 1300 SNe Ia and detect a correlation between Hubble residual and host galaxy mass at a significance of 4σ .

This effect can bias our determination of the Hubble constant if the sample of SNe Ia in CSP-I have hosts with significantly different stellar mass than the 19 hosts with Cepheid distances used to anchor the Hubble diagram. To investigate this, we determine stellar masses for a subsample of CSP-I hosts using the 2MASS extended source catalog (Jarrett et al. 2000). We then assume a constant mass-to-light ratio in the K band (McGaugh & Schombert 2014). Under this assumption, the stellar mass of a host galaxy is given by

$$\log_{10}(M_*/M_\odot) = -0.4(m_K - \mu) + C, \quad (12)$$

where m_K is the apparent K magnitude of the host, μ is its distance modulus, and C is a constant that sets the mass scale. To determine C , we apply Equation (12) to the sample of galaxies from Neill et al. (2009) that have 2MASS K -band photometry. The left panel of Figure 9 shows the comparison of the two estimates in stellar mass. The best-fit value for the mass scale is $C = -1.04$ dex, and the rms scatter is ± 0.3 dex.

Of the 120 SNe Ia in the CSP-I sample, 103 have 2MASS measurements of the host galaxy, and their K -band magnitudes and corresponding stellar masses are listed in Table 2. An additional four objects (SN 2003du, SN 2005ir, SN 2006ej, and SN 2008bf) are in the Neill et al. (2009) sample and can be used directly. Lastly, we use host mass estimates from Chang et al. (2015) for another eight objects, including the host of SN 2012ht. To check for consistency, we have plotted the Neill et al. (2009) masses versus the Chang et al. (2015) masses for 46 objects they have in common. Aside from one clear outlier, the correspondence is very good, with an rms scatter of 0.2 dex. This leaves us with only five objects for which we have no host mass estimates. These are left as free parameters with uniform priors over the range of stellar masses observed for the CSP-I sample: $9 < \log_{10}(M_*/M_\odot) < 11.5$.

The mean stellar mass of the CSP-I sample excluding the Cepheid hosts is $\log_{10}(M_*/M_\odot) = 10.7$, whereas the mean stellar mass of the Cepheid hosts is $\log_{10}(M_*/M_\odot) = 10.1$, for a difference of 0.6 dex. This is large enough to produce a 2%–3%

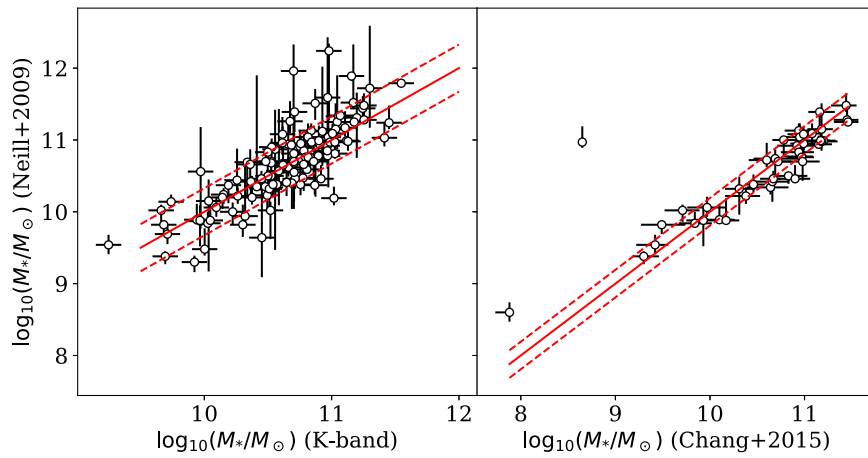


Figure 9. Comparison of host galaxy stellar masses determined from 2MASS K -band photometry (left panel) and masses from Chang et al. (2015; right panel) with those from Neill et al. (2009). The solid red lines are fits assuming a slope of 1, and the dashed lines indicate ± 0.3 dex.

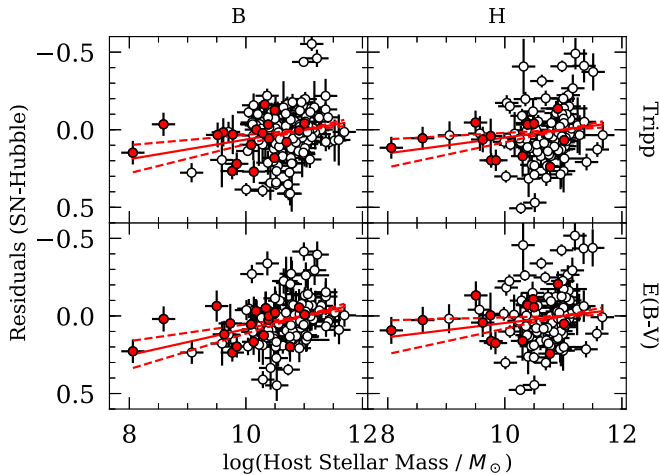


Figure 10. Residuals in the Hubble diagram as a function of stellar mass of the host galaxies. The top row of panels shows residuals from the Tripp model, while the bottom row shows residuals from the extinction method. The left column is for the B band, while the right column is for the H band. The best-fit lines are shown as red solid lines with the 1σ as dashed red lines. The SNe Ia with Cepheid distances are plotted as red points.

shift in H_0 , given the typical host mass–luminosity slopes that are measured. We therefore include a linear correction factor in Equations (4) and (7). The slopes of the host mass corrections are given in Tables 1 and 3. Figure 10 shows the correlation between Hubble residuals and host mass using two different filters (B and H) and the two different methods of treating extinction. In all cases, the slope is significant to between 1σ and 2σ , but generally decreasing with wavelength. The hosts with Cepheid distances are colored with red points.

Appendix C Intrinsic Color Model with Basis Splines

Burns et al. (2014) modeled the intrinsic color as a second-order polynomial, which therefore had three degrees of freedom per filter. There is no physical basis for this, and it was chosen primarily as a numerical convenience. Any functional form that captures the shape of the “blue edge” in Figure 3 will suffice. With additional data from CSP-I, it became apparent that a simple polynomial was insufficient.

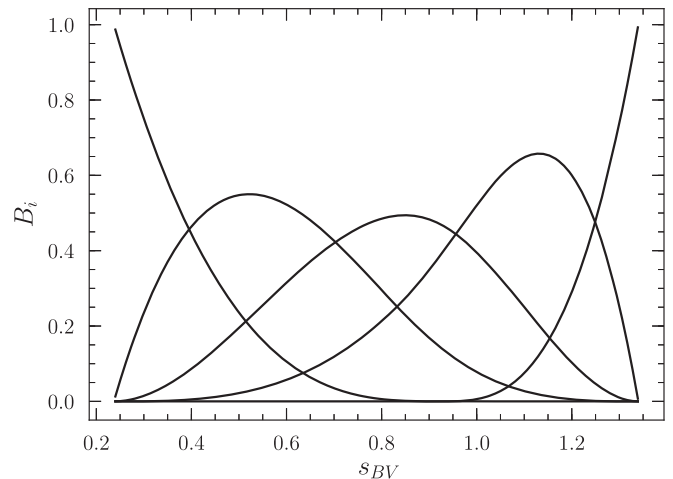


Figure 11. The five basis splines used to model the intrinsic colors of the SNe Ia.

Basis splines provide more flexibility needed to fit the complex behavior. Also, the sample of objects is sparse at either end of the luminosity–decline rate relation, and individual objects at either end of the distribution in s_{BV} will not influence the overall shape of a spline as much as it would for a polynomial.

Basis splines are constructed using basis functions:

$$S(s_{BV}) = \sum_i a_i B_i(s_{BV}). \quad (13)$$

Here S is the spline function used to model the intrinsic colors, a_i are the spline coefficients controlling the shape, and B_i are the basis functions, which are constructed recursively using the Cox–de Boor algorithm (de Boor 1978). This algorithm is available as a standard library for most scientific computing languages. The values of $B_i(s_{BV})$ can be computed for each SN Ia and then passed to STAN as data, which will solve for the a_i as free parameters of the model.

We chose knot points at $s_{BV} = [0.23, 0.9, 1.34]$, corresponding to the two endpoints of the distribution and the median value. For a cubic spline, this leads to five basis splines and therefore five degrees of freedom for each filter. Figure 11 shows the functional form of these basis functions. Table 9 lists

Table 9
Basis-spline Coefficients for Intrinsic Colors of SNe Ia

Color	a_0	a_1	a_2	a_3	a_4	σ
$u - B$	1.21(0.12)	0.77(0.14)	0.16(0.13)	0.41(0.09)	-0.08(0.15)	0.099
$B - V$	0.68(0.05)	0.21(0.05)	-0.25(0.06)	0.06(0.04)	-0.18(0.08)	0.029
$g - r$	0.43(0.07)	-0.08(0.06)	-0.24(0.07)	-0.19(0.05)	-0.40(0.10)	0.013
$V - r$	0.13(0.05)	-0.12(0.05)	-0.06(0.05)	-0.17(0.03)	-0.21(0.07)	0.019
$V - i$	0.02(0.08)	-0.51(0.07)	-0.65(0.07)	-0.90(0.05)	-0.76(0.09)	0.035
$r - i$	-0.11(0.06)	-0.39(0.06)	-0.59(0.06)	-0.73(0.04)	-0.55(0.07)	0.035
$V - Y$	0.50(0.11)	-0.60(0.10)	-0.30(0.11)	-1.20(0.08)	-0.63(0.16)	0.041
$Y - J$	0.01(0.11)	0.37(0.12)	-0.18(0.11)	0.30(0.07)	-0.03(0.13)	0.078
$J - H$	0.03(0.10)	-0.31(0.12)	-0.01(0.11)	-0.46(0.07)	-0.10(0.12)	0.073
$V - J$	0.51(0.13)	-0.23(0.13)	-0.48(0.13)	-0.90(0.09)	-0.66(0.16)	0.070
$V - H$	0.55(0.12)	-0.54(0.11)	-0.49(0.12)	-1.36(0.09)	-0.77(0.17)	0.029

the coefficients for several intrinsic colors of SNe Ia as well as the intrinsic scatter σ in each color. One can construct the spline coefficients for a color not found in Table 9 by simply adding or subtracting the appropriate coefficients for two known colors.

Appendix D CSP-I Zero-points and Their Uncertainties

In order to measure H_0 using SNe Ia, a sample of nearby objects whose hosts have independent distances is required. Due to the scarcity of such events, we must combine our CSP-I sample with others from the literature, so a significant systematic uncertainty is the error in the absolute zero-points of our photometric system. This was not presented in Krisciunas et al. (2017), so we devote this section to their estimation. They apply equally well to both the CSP-I and CSP-II filter sets.

The photometric zero-point for filter X allows us to convert from magnitudes to photon fluxes measured by the telescope and is computed as

$$zp_X = m_s + 2.5 \log_{10} \left(\frac{1}{ch} \int f_{\lambda,s} S_X \lambda d\lambda \right), \quad (14)$$

where zp_X is the zero-point for filter X, m_s is the assumed *natural* magnitude of a fundamental standard (Krisciunas et al. 2017), $ch = 1.9864 \times 10^{-8}$ erg Å, $f_{\lambda,s}$ is the spectral energy distribution (SED) of the fundamental standard in $\text{erg s}^{-1} \text{cm}^{-2} \text{Å}^{-1}$, λ is the wavelength in Å, and S_X is the total transmission (telescope, instrument, and atmosphere) for filter X.

There are several sources of error in Equation (14), which we will now estimate and combine in quadrature to get a final error in each zp_X . First, there is the choice of fundamental standard. Typically the Bohlin & Gilliland (2004b) SED of Vega is used for the set B , V , Y , J , and H , while the Bohlin & Gilliland (2004a) SED of BD + 17°4708 is used for u , g , r , and i . Two other standards from CALSPEC¹³ have B - and V -band magnitudes on the Landolt (1992) system as well as u , g , r , i magnitudes on the Smith et al. (2002) system and so can be used for our optical filters: P177D and P330E (Bohlin & Landolt 2015). Indeed, BD + 17°4708 is now known to be variable (Bohlin & Landolt 2015). Using these three different fundamental standards leads to shifts in the zero-points listed as $\delta(\text{stand})$ in Table 10. For the NIR, there is only one other CALSPEC standard that has J and H photometry on the

Persson et al. (1998) system, ξ^2 Ceti (HD 15318), which was one of the standards from Frogel et al. (1978) used by Elias et al. (1982) to calibrate their standards, which were in turn used to calibrate the Persson et al. (1998) standards. In the case of the Y band, we use Equation (D1) from Krisciunas et al. (2017) to transform the J - and H -band magnitudes of ξ^2 Ceti to a Y -band magnitude.

Second, in order to compute the natural system magnitudes m_s , we employ the color terms from Krisciunas et al. (2017) in reverse. These color terms have associated errors, leading to uncertainty in m_s , which are listed as $\delta(ct)$ in Table 10.

Lastly, there remains the error in the shape of the transmission functions $S_X(\lambda)$. As detailed in Krisciunas et al. (2017), these are constructed by multiplying the throughput of the telescope, instrument, and filters as measured by Rheault et al. (2010) with a model of the atmosphere:

$$S_X(\lambda) = R_{\text{scan}}(\lambda) A_{\text{aero}}(\lambda) 10^{-0.4k_X(\text{AM}-1)} A_{\text{tel}}(\lambda). \quad (15)$$

Here, R_{scan} is the scanned throughput of the telescope, instrument, and filter; A_{aero} is the extinction in the atmosphere due to aerosols and ozone as measured at CTIO for an airmass of 1.0 (Stone & Baldwin 1983; Baldwin & Stone 1984); k_X is the extinction coefficient for filter X; AM is the typical airmass for the CSP standard observations; and A_{tel} is a model transmission function due to oxygen and water vapor. The most important systematic uncertainty in R_{scan} is the wavelength calibration, which is estimated at ± 1 Å (Rheault et al. 2010). Using synthetic photometry, we found that the resulting error in the zero points was negligible, and we therefore ignore any errors in R_{scan} and consider only systematic errors in the atmospheric transmission.

Figure 12 shows the scans R_{scan} and the atmospheric components for two different assumed values of airmass and precipitable water vapor (PWV). It is obvious that errors in A_{aero} are more important for the optical filters, whereas errors in A_{tel} are more important in the NIR, including the i band. These errors are primarily due to the assumed value of typical airmass (AM) and PWV. As stated in Krisciunas et al. (2017), we assume AM = 1.2, which corresponds to the mode of the distribution of AM for our standard star observations. However, the distribution has a long tail to high AM, and one could argue that the median of AM is more appropriate. The median for the CSP-I observations is AM = 1.33, and we therefore take $d(\text{AM}) = 0.1$ as a possible systematic error in the assumed airmass. Using Equation (14), the errors in the

¹³ <http://www.stsci.edu/instruments/observatory/cdbs/calspec.html>

Table 10
Photometric Zero-point Errors

Filter	$\delta(\text{stand})$	$\delta(ct)$	$\delta(A_{\text{aero}})$	$\delta(AM)$	$\delta(k_X)$	δA_{tel}	$\delta(zp_X)$
<i>u</i>	0.004	0.016	0.073	0.051	0.012	...	0.091
<i>g</i>	0.005	0.003	0.013	0.019	0.005	...	0.024
<i>r</i>	0.001	0.002	0.012	0.010	0.004	0.001	0.016
<i>i</i>	0.005	0.002	0.021	0.006	0.004	0.002	0.022
<i>B</i>	0.005	0.000	0.018	0.024	0.005	...	0.031
<i>V</i> (LC-3014)	0.003	0.004	0.011	0.014	0.004	...	0.019
<i>V</i> (LC-3009)	0.006	0.004	0.011	0.014	0.004	...	0.020
<i>V</i> (LC-9844)	0.003	0.004	0.011	0.014	0.004	...	0.019
<i>Y</i>	0.040	0.001	...	0.006	0.040
<i>J</i>	0.030	0.006	...	0.025	0.040
<i>H</i>	0.020	0.002	...	0.008	0.022

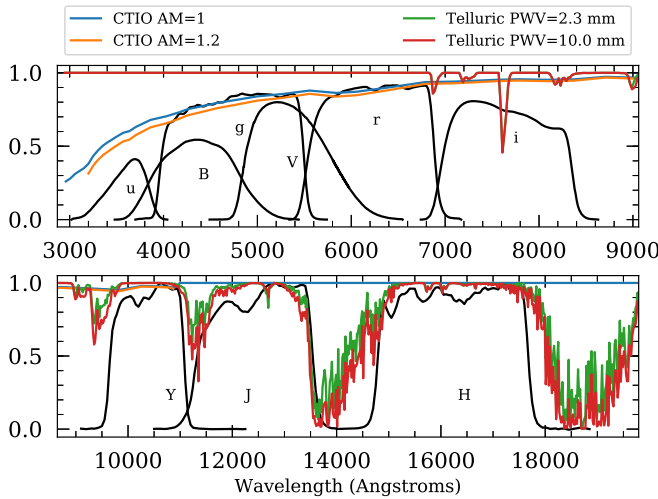


Figure 12. Scanned filter+telescope+CCD transmission lines (black curves) for optical (top panel) and NIR (bottom panel) bandpasses. The transmissions due to atmospheric effects of aerosols (blue and orange lines) and telluric lines (red and green) are plotted for two different airmasses.

zero-points due to errors $\delta(AM)$ and $\delta(K_S)$ are

$$\delta(zp_Z) = \sqrt{k_X^2 \delta^2(AM) + AM^2 \delta^2(k_X)} \quad (16)$$

and are listed in Table 10.

We now consider errors in $A_{\text{aero}}(\lambda)$ and $A_{\text{tel}}(\lambda)$. Only errors that are correlated over significant portions of the filters will be of any consequence. For $A_{\text{aero}}(\lambda)$, we have measurements of k_X as part of our CSP-I photometry, and since $k_X \sim -2.5 \log_{10} A_{\text{aero}}(\lambda_X)$, we have sampled it at nine wavelengths. To model a continuous function, we fit a Gaussian process to our observed k_X using the CTIO curve as a mean function. This allows us to generate a random sample of continuous extinction curves that are consistent with our measurements and give a representative variation in zero-point due to changes in the shape of the filter functions. These are listed in Table 10 as $\delta(A_{\text{aero}})$.

Finally, variations in $A_{\text{tel}}(\lambda)$ are very complicated and are primarily caused by changes in airmass and PWV. To model this, we use ATRAN (Lord 1992) models provided by Gemini Observatory for a variety of AM and PWV. For each, we build

new filters and determine the effects on the zero-points. As above, we allow AM to vary by ± 0.1 . For the PWV, we utilize site testing data for the Giant *Magellan* Telescope (GMTO; Thomas-Osip et al. 2010), which shows both nightly and seasonal variations of PWV. We find a median of PWV = 4.3 mm with seasonal shifts of about 2 mm. We therefore assume the “typical” PWV could be in error by ± 2 mm. The effects of these variations in AM and PWV mostly affect the NIR filters and in particular the *J* band, whose blue and red edges extend well into the water bands (see Figure 12) and whose shape is therefore influenced the most by PWV. The combined effects are listed in Table 10 as $\delta(A_{\text{tel}})$.

The final tallied error in the zero-points is listed in the final column of Table 10 and is used to model the systematic errors when combining our photometry with other systems. All filters aside from *u* are uncertain at the few percent level. The larger error in *Y* has the potential to be greatly reduced by improving the fundamental calibration. There are plans to build a small (~ 10 inch aperture) robotic telescope at LCO with NIR capabilities, which would allow us to observe brighter stars and tie the *Y* band onto the Vega system.

Appendix E Bayesian Hierarchical Models

In this appendix, we present some of the more technical aspects of our inference using Bayesian hierarchical models. A more general discussion of the numerical method used (MCMC) can be found in our earlier work on the intrinsic colors (Burns et al. 2014). We restrict discussion here to the model and priors used.

The models presented in Sections 4 and 5 are ultimately compared with observed fluxes $f_{\lambda,i}$ from the telescope. While the models were presented in magnitude units to retain their familiarity, all fitting is done in flux units. Conversion between the two is done using the standard formula:

$$f_{\lambda,i} = \exp[0.921(zp_\lambda - m_{\lambda,i})], \quad (17)$$

where zp_λ is the photometric zero-point for the telescope and filter in question. The precise values of zp_λ are not important,

as they amount to a constant change of scale (akin to a change of units), and we choose values that produce fluxes as close to unity as possible, improving numerical accuracy.

There is, however, a crucial difference between the probabilistic treatment of the Cepheid and SN photometry. Typically, fluxes measured by a photon-counting device such as a CCD are distributed as a Poisson distribution and for high enough counts approach a normal distribution. The practice of converting to magnitudes will result in a nonnormal distribution with skew toward fainter fluxes. This is the case for the SN Ia data, where one can observe the host galaxy after the SN has faded and subtract its flux entirely, leaving only the SN flux, and a normal distribution is appropriate for describing it.

For the Cepheid data, the background host light cannot be subtracted in such a way, and its contribution must be estimated in a probabilistic way by injecting multiple fake stars into the Cepheid field, measuring their recovered flux, and comparing to the injected flux (Riess et al. 2011). The resulting distribution of fluxes is dominated by fluctuations in the background galaxy light, which are found to be normally distributed in *magnitudes*,¹⁴ implying the fluxes are log-normally distributed. Log-normal distributions have a skew toward *brighter* fluxes, and if the maximum likelihood for the Cepheid photometry in magnitude units is \hat{m} , then the maximum likelihood in flux units will be $\exp(\hat{m} + \sigma^2)$, where σ is the observed standard deviation of the fake star photometry in magnitudes. The net result is a bias of order σ^2 . As part of their analysis, Riess et al. (2016) removed this bias (and other effects) from the published magnitudes, which amounts to multiplicative corrections in flux units and therefore biases the maximum likelihood in flux to *fainter* values. Using a normal distribution in this case would therefore lead to an underestimate of the flux, and since the bias corrections applied to the Cepheid data are not published, one must use a log-normal distribution (or equivalently, fit in magnitude units).

The probability of the observed Cepheid fluxes $f_{\text{ceph},i}$ given the model parameters θ is therefore

$$P(f_{i,\text{ceph}}|\theta) = \text{lognormal}(f_{i,\text{ceph}}, f_{i,\text{ceph}}^T(\theta), \sigma_{i,\text{ceph}}^2), \quad (18)$$

where $f_{i,\text{ceph}}^T(\theta)$ are the “true” Cepheid fluxes given by Equations (10) and (11). The total variance $\sigma_{i,\text{ceph}}^2$ is modeled as the sum

$$\sigma_{\text{ceph},i}^2 = \epsilon_i^2 + \sigma_{\text{ceph}}^2 + \gamma^2 \sigma_{\text{OH}}^2, \quad (19)$$

where ϵ_i^2 is the measurement error for $f_{i,\text{ceph}}$, σ_{OH} is the error in $[\text{O}/\text{H}]$, which is treated as a free parameter, and σ_{ceph}^2 is any extra variance required to explain the observed dispersion in the Leavitt law residuals. It is assumed that the errors in $f_{\text{ceph},i}$ are uncorrelated with errors in P_i or $[\text{O}/\text{H}]_i$ for the Cepheids and that errors in period P_i are negligible. However, in order to allow the model to down-weight Cepheid variables based on their period (Freedman et al. 2001), we add an extra error term

to σ_{ceph}^2 :

$$\sigma_{\text{ceph}}^2 = \sigma_{\text{ceph}}^2 + \exp(-(P - P_0)/P_{\text{low}})) + \exp(-(P_1 - P)/P_{\text{high}}), \quad (20)$$

where (P_0, P_1) is the range of observed periods, and P_{low} and P_{high} control the lower and upper limits where the extra dispersion becomes important. The reason for doing this, instead of simply setting hard limits, is that STAN needs to compute derivatives of the probability with respect to the parameters, and we therefore need an analytic (rather than Boolean) representation of the variance.

For the SNe Ia, we assume the errors in $f_{\lambda,i}$ and $z_{\text{hel},i}$ are uncorrelated. We use the measured covariance between $f_{\lambda,i}$ and $s_{BV,i}$ from the SNooPy fits and assume normally distributed errors in flux:

$$P([f_{\lambda,i}, s_{BV,i}]|\theta) = N^2([f_{\lambda,i}^T - f_{\lambda,i}, s_{BV,i}^T - s_{BV,i}], \mathcal{C}_i), \quad (21)$$

where N^2 is a 2D multivariate normal distribution centered at $[0, 0]$ and with covariance matrix \mathcal{C}_i , $f_{\lambda,i}^T$ is the true value given by Equations (4) and (7), and $s_{BV,i}^T$ are the true color-stretch values, which are nuisance parameters. As with the Cepheid data, we include a free parameter to model any intrinsic variance $\sigma_{\text{SN},\lambda}^2$ required to describe the observed dispersion in the luminosity–decline rate relation. We also include a term that takes into account the added variance due to peculiar velocities of the host galaxies that arises when using redshift to compute distances. These terms are added to the $(0, 0)$ component of \mathcal{C}_i :

$$\mathcal{C}_i(0, 0) = \epsilon_{\lambda,i}^2 + \sigma_{\text{SN},\lambda}^2 + \left(\frac{v_{\text{pec}}}{cz_{\text{cmb}}} \right)^2, \quad (22)$$

where $\epsilon_{\lambda,i}$ is the measurement error in $f_{\lambda,i}$, and v_{pec} is the typical peculiar velocity for an SN Ia host, which we treat as a free parameter.

The probability for the entire data set D is then the product:

$$P(D|\theta) = \prod_i P(f_{\text{ceph},i}|D) \prod_j P(f_{\lambda,j}|D). \quad (23)$$

Using Bayes’ theorem, the posterior of the parameters of interest is given by

$$P(\theta|D) \propto P(D|\theta)P(\theta), \quad (24)$$

where $P(D|\theta)$ is given by Equation (23) and $P(\theta)$ are the priors on our variables. Experimentation has shown that uniform priors are appropriate for all our nuisance parameters save those that involve intrinsic variances and the Cepheid period range (P_{low} and P_{high}), for which we impose strictly positive values.¹⁵ For the extinction parameters of the SNe Ia, $E(B - V)_i$ and $R_{V,i}$, we use priors based on the results of the color-based analysis detailed in Section 4.2. A

¹⁴ A. Riess (2018, private communication).














¹⁵ Note that uniform priors placed on parameters expressed in magnitudes imply Jeffreys priors in flux units.

Table 11
Bayesian Model Parameters

Parameter	Description	Prior	Typical value
SNe Ia			
H_0	Hubble constant	$U(-\infty, \infty)$	See Table 5
P_λ^N	Coefficients of the decline rate relation	$U(-\infty, \infty)$	See Tables 1 and 3
R_{XYZ}	Tripp coefficient for filter X corrected by color $Y - Z$	$U(0, \infty)$	See Table 1
$[E(B - V)_i, R_{V,i}]$	Color excess and reddening slope	See Burns et al. 2014	See Table 2
α	Slope of the host galaxy mass–luminosity correction	$U(-\infty, \infty)$	See Tables 1 and 3
v_{pec}	Peculiar velocity of SN hosts	$U(0, \infty)$	200–300 km s ^{−1}
σ_λ	Intrinsic dispersion in filter λ	$U(0, \infty)$	See Tables 1 and 3
q_i	Outlier probability of data point i	$U(0, 1)$	See Table 2
Cepheids			
$M_{\text{ceph},H}$	Cepheid absolute magnitude zero point	$U(-\infty, \infty)$	−2.59(09) mag
α	Slope of the period–luminosity relation	$U(-\infty, \infty)$	−3.24(04) mag
β	Slope of the period–color relation	$U(-\infty, \infty)$	0.30(05)
γ	Slope of the metallicity–luminosity relation	$U(-\infty, \infty)$	−0.07(09) mag dex ^{−1}
σ_{ceph}	Intrinsic dispersion	$U(0, \infty)$	0.30(01)
σ_{OH}	Uncertainty in [O/H] measurements	$U(0, \infty)$	0.78(66) dex
$P_{\text{min}}, P_{\text{max}}$	Period limits for Cepheid sample	$U(0, \infty)$	5.10(06), 98.78(04) days
q_i	Mixture fraction for data point i	$U(0, 1)$	0.65–0.80
m_c	Mixture offset for second component	$U(-\infty, \infty)$	0.14–0.25 mag
σ_c	Mixture width for second component	$U(0, \infty)$	0.25–0.71 mag

summary of all the parameters and their typical values and errors is given in Table 11.

ORCID iDs

Christopher R. Burns  <https://orcid.org/0000-0003-4625-6629>
 Emilie Parent  <https://orcid.org/0000-0002-0430-6504>
 M. M. Phillips  <https://orcid.org/0000-0003-2734-0796>
 Maximilian Stritzinger  <https://orcid.org/0000-0002-5571-1833>
 Kevin Krisciunas  <https://orcid.org/0000-0002-6650-694X>
 Eric Y. Hsiao  <https://orcid.org/0000-0003-1039-2928>
 Carlos Contreras  <https://orcid.org/0000-0001-6293-9062>
 Luis Busta  <https://orcid.org/0000-0001-9952-0652>
 Peter Heoflich  <https://orcid.org/0000-0002-4338-6586>
 Barry F. Madore  <https://orcid.org/0000-0002-1576-1676>
 Nidia Morrell  <https://orcid.org/0000-0003-2535-3091>
 S. E. Persson  <https://orcid.org/0000-0003-0554-7083>
 Francisco Salgado  <https://orcid.org/0000-0002-2162-7641>

References

- Arnett, W. D. 1982, *ApJ*, **253**, 785
 Ashall, C., Mazzali, P., Bersier, D., et al. 2014, *MNRAS*, **445**, 4427
 Baldwin, J. A., & Stone, R. P. S. 1984, *MNRAS*, **206**, 241
 Beaton, R. L., Freedman, W. L., Madore, B. F., et al. 2016, *ApJ*, **832**, 210
 Benedict, G. F., McArthur, B. E., Feast, M. W., et al. 2007, *AJ*, **133**, 2908
 Bohlin, R. C., & Gilliland, R. L. 2004a, *AJ*, **128**, 3053
 Bohlin, R. C., & Gilliland, R. L. 2004b, *AJ*, **127**, 3508
 Bohlin, R. C., & Landolt, A. U. 2015, *AJ*, **149**, 122
 Burns, C. R., Stritzinger, M., Phillips, M. M., et al. 2011, *AJ*, **141**, 19
 Burns, C. R., Stritzinger, M., Phillips, M. M., et al. 2014, *ApJ*, **789**, 32
 Buta, R. J., & Turner, A. 1983, *PASP*, **95**, 72
 Cardelli, J. A., Clayton, G. C., & Mathis, J. S. 1989, *ApJ*, **345**, 245
 Carpenter, B., Gelman, A., Hoffman, M., et al. 2017, *J. Stat. Soft.*, **76**, 1
 Cartier, R., Hamuy, M., Pignata, G., et al. 2014, *ApJ*, **789**, 89
 Chang, Y.-Y., van der Wel, A., da Cunha, E., & Rix, H.-W. 2015, *ApJS*, **219**, 8
 Contreras, C., Phillips, M. M., Burns, C. R., et al. 2018, *ApJ*, **859**, 24
 de Boor, C. 1978, *A Practical Guide to Splines* (New York: Springer)
 Dhawan, S., Jha, S. W., & Leibundgut, B. 2018, *A&A*, **609**, A72
 Elias, J. H., Frogel, J. A., Hackwell, J. A., & Persson, S. E. 1981, *ApJL*, **251**, L13
 Elias, J. H., Frogel, J. A., Matthews, K., & Neugebauer, G. 1982, *AJ*, **87**, 1029
 Filippenko, A. V., Li, W. D., Treffers, R. R., & Modjaz, M. 2001, in *ASP Conf. Ser.* 246, IAU Coll. 183: Small Telescope Astronomy on Global Scales —, ed. B. Paczynski, W.-P. Chen, & C. Lemme (San Francisco, CA: ASP), 121
 Filippenko, A. V., Richmond, M. W., Branch, D., et al. 1992, *AJ*, **104**, 1543
 Fitzpatrick, E. L. 1999, *PASP*, **111**, 63
 Folatelli, G., Phillips, M. M., Burns, C. R., et al. 2010, *AJ*, **139**, 120
 Foley, R. J., & Kasen, D. 2011, *ApJ*, **729**, 55
 Foley, R. J., Narayan, G., Challis, P. J., et al. 2010, *ApJ*, **708**, 1748
 Freedman, W. L., & Madore, B. F. 2010, *ARA&A*, **48**, 673
 Freedman, W. L., & Madore, B. F. 2011, *ApJ*, **734**, 46
 Freedman, W. L., Madore, B. F., Gibson, B. K., et al. 2001, *ApJ*, **553**, 47
 Freedman, W. L., Madore, B. F., Scowcroft, V., et al. 2011, *AJ*, **142**, 192
 Friedman, A. S., Wood-Vasey, W. M., Marion, G. H., et al. 2015, *ApJS*, **220**, 9
 Frogel, J. A., Persson, S. E., Matthews, K., & Aaronson, M. 1978, *ApJ*, **220**, 75
 Gelman, A., & Rubin, D. B. 1992, *StaSci*, **7**, 457
 Groenewegen, M. A. T. 1999, *A&AS*, **139**, 245
 Guy, J., Astier, P., Baumont, S., et al. 2007, *A&A*, **466**, 11
 Guy, J., Astier, P., Nobili, S., Regnault, N., & Pain, R. 2005, *A&A*, **443**, 781
 Hamuy, M., Folatelli, G., Morrell, N. I., et al. 2006, *PASP*, **118**, 2
 Hamuy, M., Phillips, M. M., Maza, J., et al. 1995, *AJ*, **109**, 1
 Hamuy, M., Phillips, M. M., Suntzeff, N. B., et al. 2003, *Natur*, **424**, 651
 Hicken, M., Challis, P., Kirshner, R. P., et al. 2012, *ApJS*, **200**, 12
 Hicken, M., Wood-Vasey, W. M., Blondin, S., et al. 2009, *ApJ*, **700**, 1097
 Hoefflich, P., Hsiao, E. Y., Ashall, C., et al. 2017, *ApJ*, **846**, 58
 Höflich, P., Krisciunas, K., Khokhlov, A. M., et al. 2010, *ApJ*, **710**, 444
 Hogg, D. W., Bovy, J., & Lang, D. 2010, arXiv:1008.4686
 Howell, D. A., Sullivan, M., Nugent, P. E., et al. 2006, *Natur*, **443**, 308
 Hsiao, E. Y., Conley, A., Howell, D. A., et al. 2007, *ApJ*, **663**, 1187
 Hsiao, E. Y., Marion, G. H., Phillips, M. M., et al. 2013, *ApJ*, **766**, 72
 Humphreys, E. M. L., Reid, M. J., Moran, J. M., Greenhill, L. J., & Argon, A. L. 2013, *ApJ*, **775**, 13
 Jang, I. S., Hatt, D., Beaton, R. L., et al. 2017, *ApJ*, **852**, 60J
 Jarrett, T. H., Chester, T., Cutri, R., et al. 2000, *AJ*, **119**, 2498
 Jha, S., Riess, A. G., & Kirshner, R. P. 2007, *ApJ*, **659**, 122
 Kasen, D. 2006, *ApJ*, **649**, 939
 Kasen, D., & Woosley, S. E. 2007, *ApJ*, **656**, 661

- Kattner, S., Leonard, D. C., Burns, C. R., et al. 2012, *PASP*, **124**, 114
- Kelly, P. L., Hicken, M., Burke, D. L., Mandel, K. S., & Kirshner, R. P. 2010, *ApJ*, **715**, 743
- Krisciunas, K., Contreras, C., Burns, C. R., et al. 2017, *AJ*, **154**, 211
- Krisciunas, K., Phillips, M. M., & Suntzeff, N. B. 2004, *ApJL*, **602**, L81
- Krisciunas, K., Suntzeff, N. B., Candia, P., et al. 2003, *AJ*, **125**, 166
- Landolt, A. U. 1992, *AJ*, **104**, 340
- Leibundgut, B., Kirshner, R. P., Filippenko, A. V., et al. 1991, *ApJL*, **371**, L23
- Leibundgut, B., Kirshner, R. P., Phillips, M. M., et al. 1993, *AJ*, **105**, 301
- Li, W., Filippenko, A. V., Gates, E., et al. 2001, *PASP*, **113**, 1178
- Lindgren, L., Hernandez, J., Bombrun, A., et al. 2018, *A&A*, **616A**, 2L
- Lord, S. D. 1992, A New Software Tool for Computing Earth's Atmospheric Transmission of Near- and Far-infrared Radiation, Tech. Memo. 103597 (Washington, D.C.: NASA)
- Madore, B. F. 1982, *ApJ*, **253**, 575
- Madore, B. F., & Freedman, W. L. 1991, *PASP*, **103**, 933
- Madore, B. F., Mager, V., & Freedman, W. L. 2009, *ApJ*, **690**, 389
- Mandel, K. S., Narayan, G., & Kirshner, R. P. 2011, *ApJ*, **731**, 120
- Mandel, K. S., Scolnic, D. M., Shariff, H., Foley, R. J., & Kirshner, R. P. 2017, *ApJ*, **842**, 93
- Marion, G. H., Brown, P. J., Vinkó, J., et al. 2016, *ApJ*, **820**, 92
- Matheson, T., Joyce, R. R., Allen, L. E., et al. 2012, *ApJ*, **754**, 19
- McGaugh, S. S., & Schombert, J. M. 2014, *AJ*, **148**, 77
- Nataf, D. M. 2015, *MNRAS*, **449**, 1171
- Neill, J. D., Hudson, M. J., & Conley, A. 2007, *ApJL*, **661**, L123
- Neill, J. D., Sullivan, M., Howell, D. A., et al. 2009, *ApJ*, **707**, 1449
- Oke, J. B., & Sandage, A. 1968, *ApJ*, **154**, 21
- Pan, Y.-C., Foley, R. J., Kromer, M., et al. 2015, *MNRAS*, **452**, 4307
- Perlmutter, S., Aldering, G., Goldhaber, G., et al. 1999, *ApJ*, **517**, 565
- Persson, S. E., Madore, B. F., Krzemiński, W., et al. 2004, *AJ*, **128**, 2239
- Persson, S. E., Murphy, D. C., Krzemiński, W., Roth, M., & Rieke, M. J. 1998, *AJ*, **116**, 2475
- Phillips, M. M. 1993, *ApJL*, **413**, L105
- Phillips, M. M. 2012, *PASA*, **29**, 434
- Phillips, M. M., Contreras, C., Hsiao, E. Y., et al. 2018, *PASP*, in press (arXiv:1810.09252)
- Phillips, M. M., Lira, P., Suntzeff, N. B., et al. 1999, *AJ*, **118**, 1766
- Planck Collaboration, Ade, P. A. R., Aghanim, N., et al. 2016, *A&A*, **594**, A13
- Pskovskii, I. P. 1977, *SvA*, **21**, 675
- Quimby, R., Höflich, P., & Wheeler, J. C. 2007, *ApJ*, **666**, 1083
- Rasmussen, C., & Williams, K. 2006, *Gaussian Processes for Machine Learning* (Cambridge, MA: MIT Press)
- Rheault, J.-P., DePoy, D. L., Behm, T. W., et al. 2010, *Proc. SPIE*, **7735E**, 64R
- Richmond, M. W., & Smith, H. A. 2012, *JAAVSO*, **40**, 872
- Riess, A. G., Casertano, S., Yuan, W., et al. 2018, *ApJ*, **855**, 136
- Riess, A. G., Kirshner, R. P., Schmidt, B. P., et al. 1999, *AJ*, **117**, 707
- Riess, A. G., Li, W., Stetson, P. B., et al. 2005, *ApJ*, **627**, 579
- Riess, A. G., Macri, L., Casertano, S., et al. 2011, *ApJ*, **730**, 119
- Riess, A. G., Macri, L. M., Hoffmann, S. L., et al. 2016, *ApJ*, **826**, 56
- Riess, A. G., Press, W. H., & Kirshner, R. P. 1996, *ApJ*, **473**, 88
- Sandage, A., & Tammann, G. A. 2006, *ARA&A*, **44**, 93
- Sandage, A., Tammann, G. A., Saha, A., et al. 2006, *ApJ*, **653**, 843
- Schweizer, F., Burns, C. R., Madore, B. F., et al. 2008, *AJ*, **136**, 1482
- Silverman, J. M., Foley, R. J., Filippenko, A. V., et al. 2012, *MNRAS*, **425**, 1789
- Silverman, J. M., Nugent, P. E., Gal-Yam, A., et al. 2013, *ApJS*, **207**, 3
- Smith, J. A., Tucker, D. L., Kent, S., et al. 2002, *AJ*, **123**, 2121
- Stanishev, V., Goobar, A., Benetti, S., et al. 2007, *A&A*, **469**, 645
- Stone, R. P. S., & Baldwin, J. A. 1983, *MNRAS*, **204**, 347
- Stritzinger, M., Burns, C. R., Phillips, M. M., et al. 2010, *AJ*, **140**, 2036
- Stritzinger, M., Suntzeff, N. B., Hamuy, M., et al. 2005, *PASP*, **117**, 810
- Stritzinger, M. D., Phillips, M. M., Boldt, L. N., et al. 2011, *AJ*, **142**, 156
- Stritzinger, M. D., Valenti, S., Höflich, P., et al. 2015, *A&A*, **573**, A2
- Sullivan, M., Conley, A., Howell, D. A., et al. 2010, *MNRAS*, **406**, 782S
- Thomas-Osip, J. E., Prieto, G., McWilliam, A., et al. 2010, *Proc. SPIE*, **7733**, 77334N
- Tripp, R. 1998, *A&A*, **331**, 815
- Uddin, S. A., Mould, J., Lidman, C., Ruhlmann-Kleider, V., & Zhang, B. R. 2017, *ApJ*, **848**, 56
- Wang, X., Li, W., Filippenko, A. V., et al. 2009, *ApJ*, **697**, 380